Chemical Engineering Journal 543 (2026) 177992

Contents lists available at ScienceDirect

Chemical Engineering Journal

journal homepage: www.elsevier.com/locate/cej

Conceptual design and experimental validation of a novel pilot-scale crystallizer for $Mg(OH)_2$ recovery from concentrated saline solutions

Ferdinando Miciletta [a], Giuseppe Battaglia [a,*], Fabrizio Vicari [b], Fabrizio Vassallo [b], Daniele Marchisio [c], Alessandro Tamburini [a], Andrea Cipollina [a], Giorgio Micale [a]

[a] Dipartimento di Ingegneria, Università degli Studi di Palermo, Palermo, Viale delle Scienze ed 6, 90128, Italy
[b] ResourSEAs SrL, Via Notarbartolo n. 38, Italy
[c] Department of Applied Science and Technology, Politecnico di Torino, C.so Duca degli Abruzzi 24, 10129, Torino, Italy

ARTICLE INFO

Keywords:
Magnesium hydroxide
Pilot scale
CFD simulation
Mineral recovery
Precipitation
Brine valorisation

ABSTRACT

Reactive crystallization of magnesium hydroxide from concentrated saline solutions represents an effective route for magnesium recovery yet being challenging due to the complexity in controlling crystallization phenomena. This study presents the numerical model–guided design and experimental validation of an innovative pilot-scale crystallizer, the Multiple Feed Plug Flow Reactor (MFPFR). The reactor configuration was optimized through CFD simulations with local supersaturation analysis, identifying the hydrodynamic conditions that minimize local supersaturation peaks, thereby slowing nucleation processes and promoting crystal growth. The prototype was then constructed and tested using concentrated bitterns ($[Mg^{2+}] \approx 2$ M) and 0.5 M NaOH solution as alkaline reagent. The produced $Mg(OH)_2$ suspensions exhibited excellent solid–liquid separation performance, with initial settling velocities up to 440 mm/h and filtration rates above 80 kg/(m^2·h), outperforming literature data. The obtained solids showed a high degree of crystallinity, while the overall process achieved magnesium recoveries exceeding 99%. These results demonstrate the effectiveness of the integrated modeling–experimental approach and confirm the potential of the novel MFPFR for high-quality $Mg(OH)_2$ production from concentrated saline streams.

1. Introduction

Magnesium hydroxide, $Mg(OH)_2$, is an inorganic compound widely employed as a flame-retardant filler in polymeric matrices [1–3], a neutralizing agent in wastewater treatment [4,5], a material for CO_2 capture strategies [6], etc. Reactive crystallization (or precipitation) under ambient temperature and pressure is one of the most widely adopted methods for synthesizing magnesium hydroxide (MDH) from Mg^{2+}-containing solutions [7]. This approach is cost-effective and easy to implement. During precipitation, magnesium ions (Mg^{2+}) react with an alkaline solution, leading to the near-instantaneous nucleation of MDH particles, owing to its low solubility in water. Despite its simplicity, this technique presents several challenges related to the use of the produced suspension: (i) poor thickening performance, (ii) low filtration rates, and (iii) difficulties in controlling particles morphology. These represent the major drawbacks to industrial MDH production though precipitation.

Song et al. [8] analyzed the influence of the use of different reactor configurations, i.e. single feed and double feed semi-batch arrangements, on the filtration rate of MDH slurries produced from a 2 M artificial magnesium chloride, $MgCl_2$, and a 4 M sodium hydroxide, NaOH, solutions. Filtration times ranged from 2 to 3 h (estimated magma density of 58.3 g/L) in single feed semi-batch tests; while filtration times were lower than 3 min in double-feed semi-batch ones. However, since the authors did not specify the filtration conditions, it is not possible to derive an area-normalized filtration rate for comparison purposes.

Henrist et al. [9] explored the influence of different alkaline reagents and magnesium sources on the MDH precipitation in double-feed tests, namely a 1.5 M NaOH and 1.5 M ammonium hydroxide (NH_4OH) solutions, using either 0.75 M magnesium chloride ($MgCl_2$) or magnesium sulfate ($MgSO_4$) solutions. The addition of the NaOH agent, a strong base, raised pH values above 13, observing the formation of globular particles; conversely, hexagonal platelets were produced using NH_4OH solutions, due to the buffer action of ammonia solution (pH values around 10). However, despite its advantages in morphology control, the use of ammonia raises safety concerns due to its volatility and toxicity.

* Corresponding author.
E-mail address: giuseppe.battaglia03@unipa.it (G. Battaglia).

https://doi.org/10.1016/j.cej.2026.177992
Received 25 February 2026; Received in revised form 11 May 2026; Accepted 1 June 2026
Available online 24 June 2026

On the contrary, when magnesium sulfate was used as the precursor in combination with the NH_4OH solution, the particles appeared highly agglomerated, likely due to the weakly basic nature of sulfate ions, which increased supersaturation and promoted rapid nucleation and agglomeration.

Several other works have investigated the precipitation of MDH from real Mg^{2+}-containing solutions.

Turek et al. [10] studied MDH recovery from hard coal mine brines using NaOH solutions in a single feed semi-batch reactor. The authors reported settling rate of 120 mm/h and filtration rate of 7 kg/m^2 h. These values are notably low, indicating poor separation efficiency. [11]. Dong et al. [11] studied the precipitation process of MDH from rejected brines (Mg^{2+} concentration equal to 1.7 g/L) from a desalination plant in Singapore. The authors observed intense particle aggregation and undesirable granular morphology using a highly concentrated 16 M NaOH solution added in a batch reactor. Cipollina et al. [12] investigated the recovery of MDH from real bitterns from saltworks (0.9 M in Mg^{2+} ions) using 2 M NaOH solutions as the alkaline source. Precipitation tests were conducted in semi-batch and continuous stirred tank reactors. The authors noted the establishment of highly agglomerated particles characterized by extremely low settling and filtration characteristics. This was attributed to the use of highly concentrated reactants.

Supersaturation, S, is a key parameter that can explain and relate MDH filtration, settling and morphology features. Supersaturation is the driving force of crystallization/precipitation processes that rules crystallization phenomena such as nucleation, growth and aggregation [13].

Yuan et al. [14] investigated the correlation between supersaturation and the nucleation and growth rates of $Mg(OH)_2$ from highly dilute solutions ($[Mg^{2+}] \approx 9 \times 10^{-4}$ M and $[OH^-] \approx 1.5 \times 10^{-3}$ M). Despite the use of such dilute system, theoretical calculations yielded average supersaturation values ranging from approximately 1.8×10^3 to 7×10^3 at ambient temperature. Under these conditions, the authors reported that both nucleation and crystal growth follow first-order kinetics, exhibiting comparable rates within the investigated regime. Alamdari et al. [15] performed a similar investigation starting from a highly concentrated solution (seawater bittern, $[Mg^{2+}] \approx 1.2$ M). The study revealed that the nucleation depends on the cube of S, while crystal growth follows a linear dependence on S, making it the rate-limiting step in the process. As a result, when highly concentrated solutions are used and supersaturation is not properly controlled, the system tends to generate a large population of fine, poorly grown particles.

Focused on supersaturation, Romano et al. [16] analyzed the influence of supersaturation on the MDH precipitation process using a semi-batch system with a double injection of $MgCl_2$ and NaOH solutions. The authors roughly estimated supersaturation under different operating conditions. Hexagonal MDH platelets were successfully produced in selected low supersaturation conditions ($S \approx 2.5$–190), although concentrated NaOH (1–2 M) solutions were adopted. The work highlighted the need for a quantitative assessment of supersaturation to thoroughly control the MDH process, especially in complex or large-scale reactors.

In this context, Computational Fluid Dynamics (CFD) is as a powerful tool that can integrate fluid dynamics and chemical reaction description, providing spatially resolved supersaturation values for the support of crystallization phenomena estimation [17] [18] [19]. In 2000, Piton et al. [20] employed a CFD tool coupled with the Four-Environment Generalized Micromixing (4-EGM) model to simulate the precipitation process of fine particles. Local turbulence and micromixing levels had a dominant impact in controlling nucleation. One year later, Wei et al. [17] numerically investigated the barium sulfate crystallization process in a semi-batch system using a CFD-Population Balance Equation (PBE) model. The authors observed that nucleation and growth phenomena took place mainly in few parts of the reactor volume, where supersaturation levels depend on reactant injection arrangement and agitation speed. Tang and Rigopoulos [21–23], investigated the reactive crystallization of barium sulfate in a T-mixer through Direct Numerical Simulation (DNS). One of the most significant findings of their work is the oscillatory nature of nucleation, arising from the strong non-linear dependence of the process on local supersaturation. Turbulent fluctuations modulate the local concentration fields, giving rise to bursts of nucleation events that occur fluctuating in space and time. Despite the highly detailed description of the phenomena, such an approach entails an extremely high computational cost, which is rarely sustainable in engineering design practice, especially for pilot or industrial scale units. Recently, Lin et al. [24] performed a CFD analysis of a rotating liquid film reactor (RLFR) for $Mg(OH)_2$ synthesis, focusing on multifluid mixing and reactor geometry optimization. Their model aimed at evaluating the effect of hydrodynamics and mixing efficiency on product yield under different operating conditions, without specifically addressing the crystallization regime or the evolution of supersaturation. Raponi et al. [25] analyzed the design of a pilot scale crystallizer for the production of $Mg(OH)_2$ at semi-industrial scale from concentrated Mg^{2+} solutions. The authors extended a CFD approach coupled with PBE model previously developed to determine precipitation kinetics of $Mg(OH)_2$ in a T-mixer [26]. The authors evaluated the impact of mixing and reagent concentration in the pilot-scale reactor focusing on their effect on the zeroth moment of the particle size distribution (PSD) and supersaturation levels. Reported supersaturation peaks ranged between approximately 10^3 and 10^4, highlighting the highly spatially heterogeneous nature of the precipitation environment. In agreement with these modeling outcomes, Battaglia et al. [27] conducted an experimental campaign testing a pilot scale crystallizer with a similar geometry to that simulated by Raponi [25] employing saltworks bitterns mixed with 0.5 M NaOH solutions. Highly pure MDH particles (mass purity >99%) were obtained with a Mg^{2+} recovery nearly 100%. Nevertheless, the corresponding suspension showed extremely poor filterability and thickening behavior, which was ascribed to the formation of globular nanosized particles, induced by the very high supersaturation in the reaction environment.

With this respect, the present work addresses the design optimization, construction, and experimental characterization of a novel pilot-scale reactive crystallizer, based on ResourSEAs original concept [28], for the synthesis of magnesium hydroxide (MDH) from Mg^{2+} concentrated solutions, such as real bitterns. The crystallizer was proposed to overcome the limitations highlighted in previous works, with a specific focus on controlling particle morphology and improving the sedimentation and filtration performance of the suspensions. Based on theoretical knowledge and practical expertise, an innovative reagent dilution and injection strategy was formulated and assessed through a numerical approach based on CFD simulations coupled with micromixing models. The optimal configuration identified through the CFD-based analysis was implemented in the Multiple *Feed Plug Flow Reactor* (MFPFR), which was constructed and experimentally tested by the University of Palermo and ResourSEAs Srl. The concept of this new reactor lies at the core of the MareMag LIFE European project [29], where a 100 t/y demonstration unit is currently under development, and is expected to provide the foundation for further industrial scale-up of magnesium hydroxide production from saline solutions. From an economic point of view, the very good solid-liquid separation performance of the MFPFR reactor enables the technology to be implemented in industrial scenarios. In fact, the faster the settling and filtration rates of suspensions the lower the footprint of settlers and filter areas, lowering unit costs. Regarding the implementation of the MFPFR technology in treatment chains for Mg^{2+}-concentrated solutions, Scelfo et al. [30] conducted an economic analysis of a treatment chain treating saltworks Sicilian bitterns encompassing an ultrafiltration unit, to remove suspended organic matter, a pH Swing Adsorption unit, for the selective extraction of boron, a magnesium crystallization reactor (the MFPFR reactor, also named Mg-CGCR within the framework of the EU SEArcularMINE project), thickeners, a drum filter, to separate $Mg(OH)_2$ solids, a pH Swing Adsorption unit, to remove all remaining divalent cations, an Electro-Dialysis with Bipolar Membranes pilot, to produce both acidic

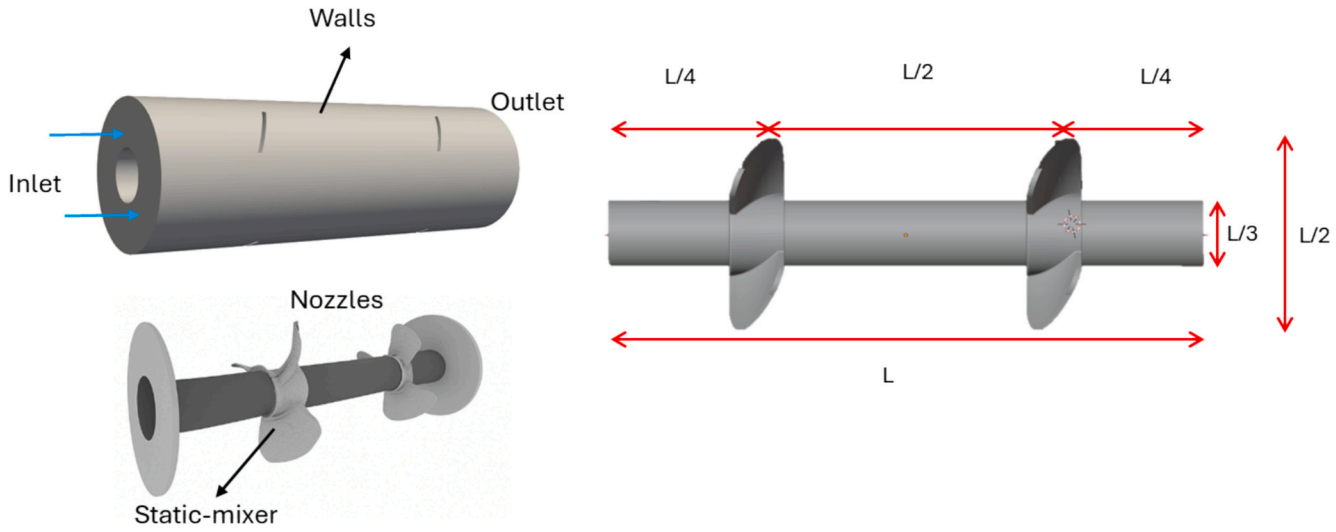

Fig. 1. 3D drawing of a section of the tubular MFPFR prototype. The sizes of the simulated reactor are expressed as a function of the total device length, L (red lines).

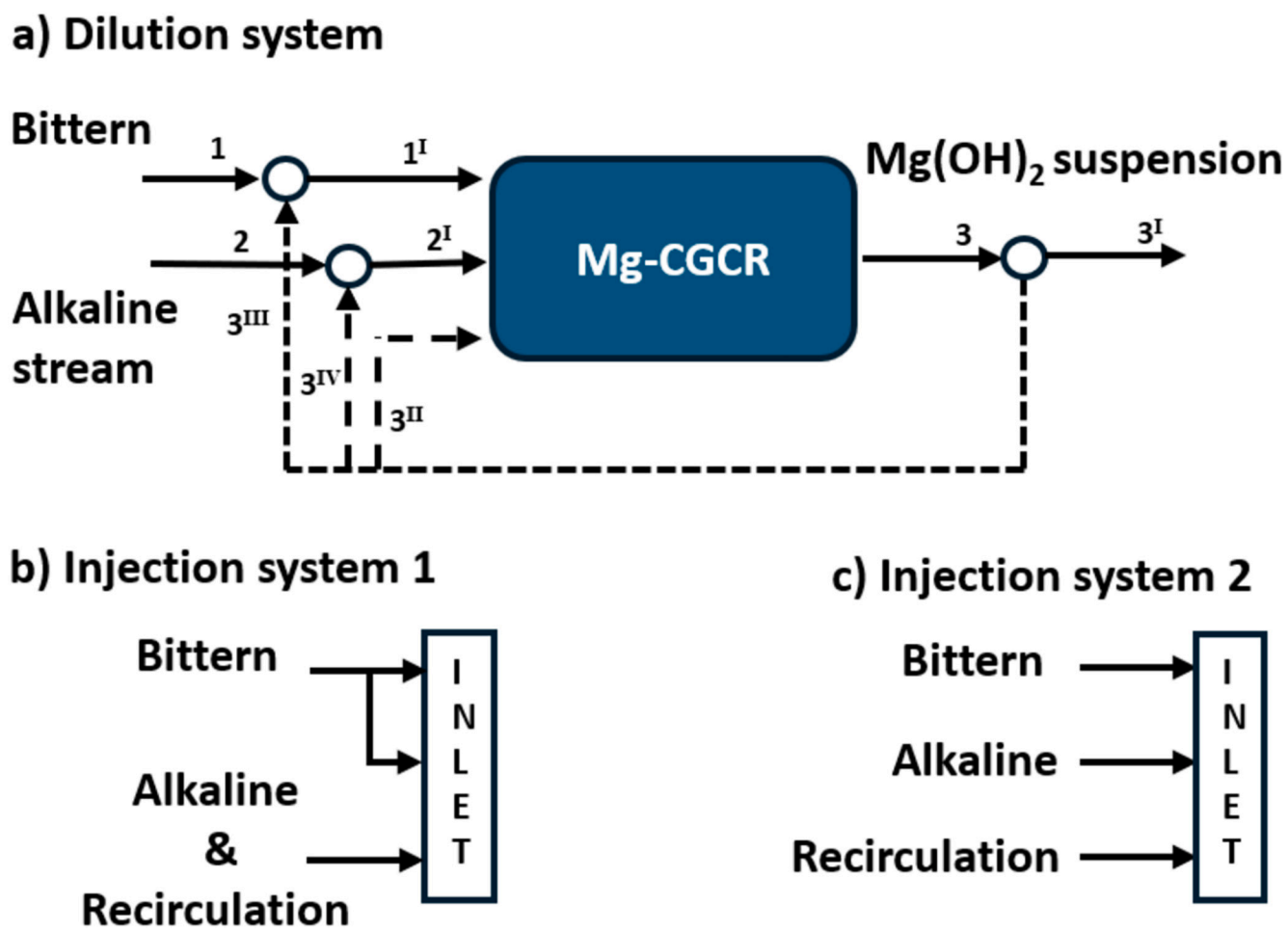

Fig. 2. Schematic representation of the dilution system employed in the MFPFR concept (a), and conceptual representations of "Injection configuration 1" (b) and "Injection configuration 2" (c).

and basic solutions in situ, a Reverse Osmosis unit, for freshwater recovery. The analysis demonstrated the economic feasibility of the treatment chain, resulting in a $Mg(OH)_2$ production cost of < €2/kg at pilot scale and < €1/kg at industrial scale, in line with market prices.

2. Reactor concept

As an evolution of the concept of the 1st MFPFR prototype [25,27,31], the geometry of the 2nd MFPFR was based on a tubular system composed of two coaxial pipes, where reactants can be injected

through nozzles into annular region. To enhance mixing, static elements shaped like marine propellers were included, generating a swirling motion within the annular volume. The three-dimensional geometry of the MFPFR prototype is shown in Fig. 1, where all reactor sizes are normalized with the overall device length, *L*.

A novel dilution strategy and two alternative injection configurations of reagents were explored to reduce and control the local supersaturation level in the reaction environment. Fig. 2 presents a schematic representation of the new dilution strategy (a) and a conceptual description of two possible injection configurations (b,c).

Regarding the dilution strategy, part of the produced $Mg(OH)_2$ suspensions is expected to be recirculated back to the inlet section, being mixed with the bittern (stream 3^{III}) and/or the alkaline solution (stream 3^{IV}). In addition, the recirculating suspension could be fed to reactor annular region to dilute the reaction environment (stream 3^{II}). As far as the injection configuration is concerned, two operative configurations may be employed: (a) the bittern stream (1^{I}) is injected through nozzles, while the alkaline solution (2^{I}), mixed with the recirculating suspension (3^{IV}), is fed through a larger manifold directly to the annular reactor volume (no need of stream 3^{II}); (b) the bittern (1^{I}) and the alkaline solution (2^{I}) are both fed through nozzles, while the recirculated suspension (3^{II}) is fed to the annular region through the larger manifold.

3. Modeling framework

Computational fluid dynamics (CFD) simulations were employed to explore the performance of the novel MFPFR prototype strategies for magnesium hydroxide precipitation. Crystallization phenomena, e.g. nucleation, growth or aggregation, as well as reactants consumption and population balance equations were not implemented due to computational and time requirements deemed to be excessive during the design of the prototype where several operating conditions and geometry configurations were analyzed. The goal was not to reproduce an existing unit, but to design and assess a virtual prototype, thus guiding the construction of a real unit. The selected geometry of the MFPFR prototype followed a preliminary numerical investigation aimed at exploring the influence of construction and operating parameters, e.g. the choice of the static mixing elements, the position of nozzles and number of nozzles. Section S1 in the Supporting Information reports the rationale behind the design of the MFPFR prototype.

3.1. Numerical details

Numerical simulations were carried out using the open-source platform OpenFOAM. The *twoLiquidMixingFoam* solver, coupled with the *PIMPLE* algorithm, was employed. Simulations were conducted within the Reynolds-Averaged Navier–Stokes (RANS) framework, adopting the k-ω SST (*Shear Stress Transport*) turbulence model, providing accurate representation of fluid flow in the system at low computational demand. The reactor domain, shown in Fig. 1, was discretized into computational cells using the *SnappyHexMesh* utility of OpenFoam. A grid independence analysis was carried out to ensure numerical accuracy, leading to a final mesh of ~3.6 million cells, 98% of which were hexahedral.

The β-Probability Density Function (β-PDF) micromixing model was implemented, following the procedure presented in Raponi et al. [26], to account for micromixing (molecular-scale interactions between reactive species). This is essential when precipitation processes of sparingly compounds, as $Mg(OH)_2$, are considered to properly evaluate supersaturation levels in the reaction environment considering the actual local concentration of reactive species available at the molecular scale. On this basis, supersaturation, *S*, was calculated as follows [14,26]:

$$S = \frac{\gamma_{\pm}^{3}\left(\overline{C}_{Mg^{2+}} \bullet \overline{C}^{2}{}_{OH^{-}}\right) - k_{sp}}{k_{sp}} \quad (1)$$

where $\overline{C}_{Mg^{2+}}$ *and* $\overline{C}_{OH^{-}}$ are the effective concentrations of magnesium and hydroxyls ions at molecular scale, k_{sp} is the solubility product constant of magnesium hydroxide, equal 5.61×10^{-12} [mol^3/L^3] at room temperature [16], and $\gamma_{\pm}$ is the mean activity coefficient of ions calculated following the Bromley's theory [32].

Boundary conditions were defined for the inlets, outlet, and wall regions of the computational domain. In particular, uniform velocity and species concentration were imposed at all inlets, while turbulence quantities (*k* and *ω*) were derived from the reference flow velocity assuming a turbulence intensity of 5% [33]. Zero gradient conditions were applied to all transported variables at the outlet, except for pressure, which was fixed to a reference value of 0. Reactor walls were treated as no-slip boundaries, and standard wall functions were adopted for turbulence quantities. Simulations were stopped once a statistically steady state was achieved, assessed through the stabilization of key monitored quantities over consecutive time steps and residuals consistently below 10^{-6}. This configuration ensured numerical stability and physical consistency in reproducing flow, mixing, and reactive transport within the MFPFR geometry.

3.2. Simulation campaign

Several different operating conditions were explored in the numerical study in terms of type of the injection configuration, (see Fig. 2 for further details) Mg^{2+} and OH^- flow rates and concentrations before and after pre-dilution with recirculating magnesium hydroxide slurry, as reported in Table 1.

A 2.0 M Mg^{2+} concentration was chosen as the representative Mg^{2+} content in bitterns produced in saltworks [34], while the alkaline solution concentration of 0.5 M was the expected one that can be produced in situ by an Electrodialysis with Bipolar Membrane unit as it has occurred in the SEArcularMINE [35] and MareMag LIFE treatment chains. Cases N1 and N2 explored the influence of the pre-dilution of the bittern solution when adopting the Injection configuration 1. In this case, the higher flow rate of the diluted Mg^{2+} solution was expected to lead to an intensification of the local turbulence near the nozzle locations. Cases N3 and N4 analyzed the use of the Injection configuration 2 with and without a pre-dilution of both NaOH and bittern solutions.

It is worth noting that, in all cases, the flow rate of solutions/suspensions flowing in the annular section (recirculating streams) was ~130 L/min.

3.3. Numerical results

Spatial distribution maps of Mg^{2+} concentrations at the outlet cross-section of the reactor geometry, and the Mg^{2+} concentration volumetric distribution (not a cumulative distribution) in the reactor are presented in Fig. 3 for all numerical cases. In Fig. 3b, the x-axis reports the local Mg^{2+} concentration that occupy a certain reactor volume fraction (the y-axis). Therefore, the curves provide a quantitative indication of how the Mg^{2+} concentration is distributed throughout the reactor volume.

Magnesium concentration was quite well distributed in most of the outlet section areas in Cases N1, N2 and N4 reaching values lower than 20 mol/m^3 (100 times lower than the inlet value of 2000 mol/m^3), indicating a good Mg^{2+} dilution in the annular section. Conversely, a localized high Mg^{2+} concentration plume can be observed in case N3, with peak values over 250 mol/m^3. This can be mainly attributed to the lower flow rate of the non-pre-diluted Mg^{2+} solution of Case N3 with respect to the pre-diluted one of case N4. Interestingly, this result was not observed in Case N1, which had the same non-pre-diluted Mg^{2+} flow rate of case N3. This is related to the different injection configurations adopted in the two simulations. Specifically, in the first injection configuration, only the bittern solution was fed in the annular region through spatially equally distributed nozzles, thus guaranteeing a good distribution of the reagent, despite the low flow rate. Conversely, in the

second injection configuration, both the alkaline solution and the Mg^{2+} reactants were fed into annular region, affecting their distribution efficiency in space. Mg^{2+} concentration maps of Cases N3 and N4 also indicate that an increase of the flow rate of the bittern solution, using the Injection configuration 2, favored the dilution of the reagent in the reaction environment, due to the higher local fluid flow regime in the system. This can be further observed in Mg^{2+} concentration distribution values evaluated within the annular volume of the reactor, see Fig. 3 (b). Higher local Mg^{2+} concentration values were reached in Cases N1 and N3, up to two orders of magnitude higher, with respect to Cases N2 and N4, due to the use of lower non-pre-diluted bittern flow rates. As a matter of fact, higher flow rates induced a more effective pre-dilution of the Mg^{2+} solution leading to lower concentration values in the system. Lower local reactant concentrations are expected to lead to low local supersaturation levels, favoring the growth of particles, thus limiting the nucleation of tiny ones [20]. On the other hand, high flow rates of the reactants can also negatively affect local crystallization kinetics due to increased fluid shear stresses that can possibly enhance aggregation or breakage phenomena [36]. Fig. 4 presents (a) the spatial distribution maps of OH^- at the outlet cross-section of the reactor and (b) the volumetric concentration of OH^- distribution maps.

The alkaline solution was almost homogeneously distributed in Cases N1 and N2 thanks to the pre-dilution action of stream 3^{IV}, which is characterized by a significantly higher flow rate than the alkaline one, leading to a low and uniform OH^- concentration throughout the reactor. Conversely, in Cases N3 and N4 concentrated and localized OH^- plumes can be observed, due to the different injection configuration. Higher localized OH^- concentrations were found in Case N3 with respect to case N4 as a result of the dilution action of the higher NaOH solution flow rate selected in case N4. As also discussed above for the bittern solution, the use of a higher reactant flow rate led to (i) lower local OH^- concentration values and (ii) a better distribution of the reactant in the annular section. The observation of the volumetric concentration distribution maps of OH ions (see **Fig. 4**b) confirms the above considerations. In Cases N1 and N2, OH^- concentrations were lower than in Cases N3 and N4 with an average value of 10 mol/m^3 throughout most of the reactor volume. Cases N3 and N4 exhibited similar OH^- distribution patterns within the reactor volume, with slightly lower concentrations in Case N4 due to the dilution effect of the higher NaOH solution flow rate.

Mg^{2+} and OH^- local concentration can be adopted to estimate local supersaturation level in the reactor to provide essential guidelines for the precipitation phenomena of $Mg(OH)_2$.

Fig. 5 shows (a) spatial distribution maps of supersaturation in the outlet cross-section of the reactor and (b) the volumetric distribution of micromixing-based supersaturation values (Eq.1).

At the outlet section of the reactor, the highest supersaturation values were attained in Cases N2 and N4. Only a very small, localized plume was observed in Case N3, indicating a poor macromixing of the reactants in the reaction volume. This was confirmed by Mg^{2+} and OH^- concentration maps reported in Figs. 3 (a) and 4 (a), where Mg^{2+} and OH^- lay opposite region of the reactor, thus being in contact, and micromixed, only in a very small part of the section of the reactor where supersaturation was established.

Volumetric distribution of supersaturation, shown in Fig. 5 (b), agreed with those evaluated at the outlet section of the reactor. Cases N2 reported the highest supersaturation values all over the reaction volume, reaching a peak value of ~3500, while Case N1 showed lower supersaturation values, with a maximum peak of about 650. This result indicates a prevalent effect of the higher local fluid flow regime, and thus higher turbulent energy dissipation, especially close to the nozzle regions, attained in Case N2 that enhances micromixing, leading to overall higher supersaturation values in the reactor volume, despite the lower local concentrations.

Although case N4 showed supersaturation levels slightly lower than those of Case N1, concentration profiles of Mg^{2+} and OH^- within the reactor differed significantly between these two configurations. To better interpret these differences, the axial evolution of the cross-section averaged supersaturation is shown in Fig. 6.

Whereas the outlet maps represent a local snapshot, the axial evolution of S identifies the position of supersaturation onset and the axial region over which reactants are effectively co-present across the section. Importantly, the onset of S must be interpreted considering the injection strategy, as shown before. Accordingly, Fig. 6 shows that Cases N1 and N2 develop a pronounced rise of S around the Mg^{2+} injection plane, where the supersaturation reaches its maximum. Most notably, supersaturation in Case N3 remains close to 0 even after the nozzles section, demonstrating that co-injection strategy alone is not sufficient. Macromixing limitations still prevent the contact of Mg^{2+} and OH^-, in agreement with the confined plume observed at the outlet. In contrast, Case N4 shows a gradual and controlled increase of S in the last portion of the reactor, indicating that the Injection configuration 2 strategy effectively mitigates segregation. Specifically, Case N1 can be described as a single-feed system, in which the bittern is injected into the annular section where OH^- species are already well diluted through the reactor volume by the pre-diluting action of the recirculating $Mg(OH)_2$ suspension. In contrast, the Injection configuration 2 strategy resembled a double-feed one, where both the NaOH and bittern solutions are injected separately. In this latter case, the pre-dilution action of the recirculating $Mg(OH)_2$ suspensions, along with their further dilution in the annular region, avoided the direct contact of highly concentrated reagents, thus controlling local micromixing and supersaturation levels. This condition is expected to favor the growth of $Mg(OH)_2$ crystals over nucleation [37].

4. Reactor design, construction and experimental validation

Although the numerical investigation did not account for reagent consumption in the reactor volume, since crystallization phenomena and population balance equations were not computed, the supersaturation analysis provided robust design-oriented insights. Among the investigated conditions, Case N4 provided the most favorable supersaturation distribution, and it was therefore adopted as the reference configuration for the design and construction of the MFPFR prototype. As explained above, the lower supersaturation of case N3, see Fig. 5 (b), is mainly due to a poor macromixing of the reactants in the reaction volume, as can be seen in Figs. 3 (a) and 4 (a), where Mg^{2+} and OH^- lay opposite region of the reactor, touching only in a very small part of the section of the reactor.

4.1. The MFPFR prototype

The skid of the MFPFR prototype, designed by ResourSEAs and built at the University of Palermo, is shown in Fig. 7.

The skid included the tubular reactor along with the piping and instrumentation systems required to operate the reactor. Bittern and alkaline solutions were handled by a gear (TEOREMA FG213) and a regenerative turbine pump (TEOREMA HTP—C), respectively. Streams 3^{II}, 3^{III} e 3^{IV} were handled by three regenerative turbine pumps (TEOREMA models PCM 3 × 12 (3^{II}), PCM 1.5 × 5 (3^{IiI}) and PCM 2.5 × 6 (3^{IV}). Flow rates were monitored using electromagnetic flow meters (KROHNE 4100C and 4300C). A pH meter (KROHNE pH 8320) was installed at the reactor outlet to monitor the pH value of the produced $Mg(OH)_2$ suspension. All instruments were connected to an NI cDAQ-9189 chassis for Ethernet-based signal acquisition and control via a LabVIEW software interface. The novel prototype was built to handle reagents and $Mg(OH)_2$ suspensions in accordance with all injection and dilution systems discussed in Section 2, (Fig. 2).

4.2. Experimental cases

A real bittern collected from Margi saltworks (Trapani, Italy) was

Table 1
Summary of operating conditions adopted in numerical simulation: injection configuration, Mg^{2+} solution flow rates and concentrations before and after pre-dilution (S.1 and S·1^{I}), OH^{-} solution flow rates and concentrations before and after pre-dilution (S.2 and S·2^{I}). Injection configuration and name of streams refer to Fig. 2. In all cases, the flow rate of solutions/suspensions flowing in the annular section (recirculating streams) was ~130 L/min.

Cases	Inj. conf.	S. 1 [L/min]	S. 1^{I} [L/min]	Mg^{2+} conc. (S.1) [M]	Mg^{2+} conc. (S. 1^{I}) [M]	S.2 [L/min]	S. 2^{I} [L/min]	OH^{-} conc. (S.2) [M]	OH^{-} conc. (S. 2^{I}) [M]
N1	1	0.33	0.33	2.00	2.00	2.65	130	0.5	0.0102
N2	1	0.33	10.66	2.00	0.0625	2.65	130	0.5	0.0102
N3	2	0.33	0.33	2.00	2.00	2.65	2.65	0.5	0.500
N4	2	0.33	5.33	2.00	0.125	2.65	5.33	0.5	0.250

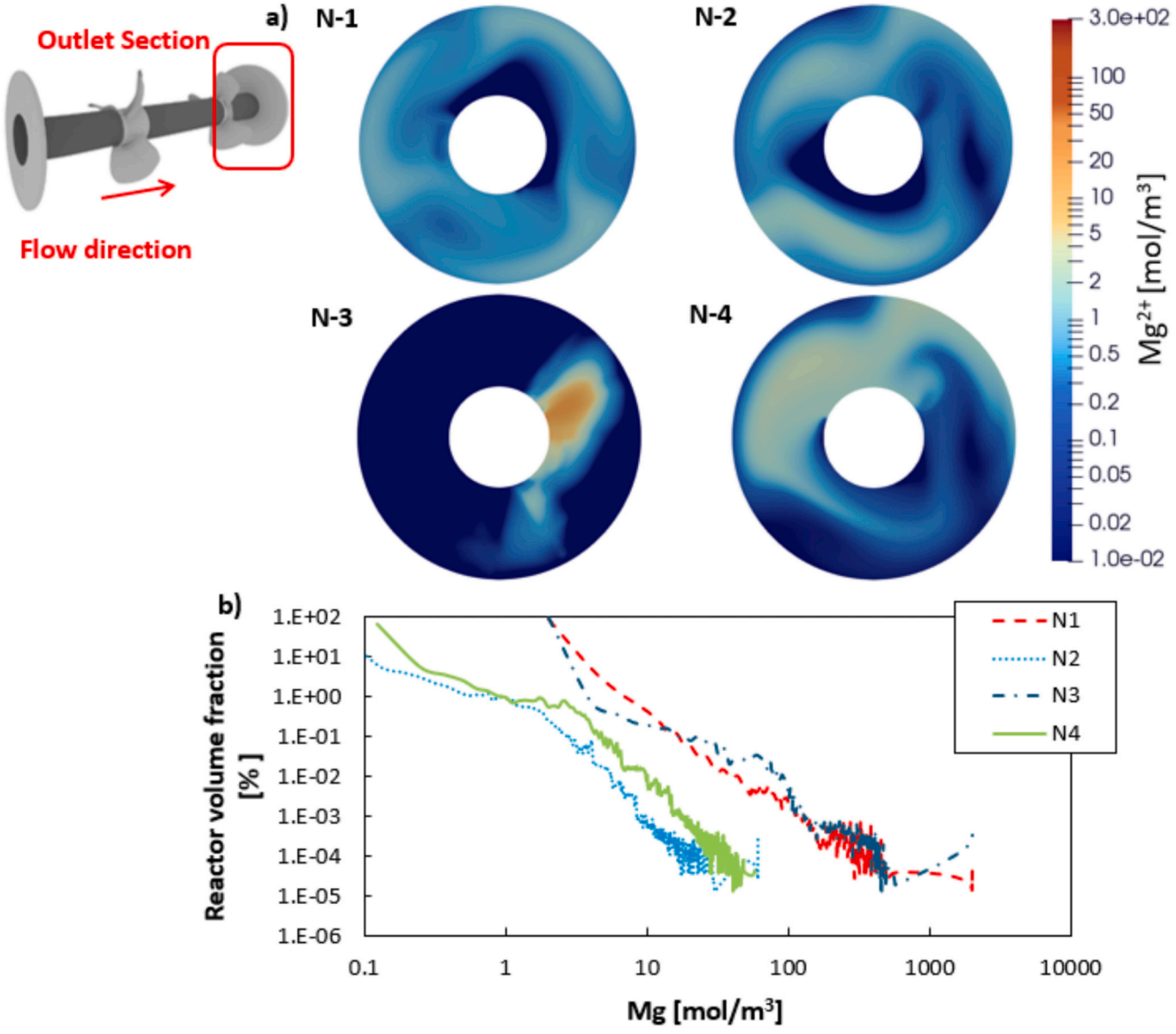

Fig. 3. (a) Concentration maps of Mg^{2+} ions at the reactor outlet section and (b) volumetric distribution (no cumulative) of Mg^{2+} ion concentration throughout the reactor.

tested in the experimental campaign. Table 2 lists the concentration of macro and micro components in the bittern. The concentrations of the components were evaluated through Ion Chromatography technique (IC, Metrohm 882 compact IC plus), Inductively Coupled Plasma Optical Emission Spectroscopy (ICP-OES, PerkinElmer Optima 2100 DV) and complexometric titration with ethylenediaminetetraacetic acid (EDTA).

Table 3 reports operating conditions explored. In the experimental campaign, the influence of the reaction pH, from a value of 10.2 to 12.7, was investigated by varying the flow rate of the inlet NaOH solution. pH interval spans from stoichiometric OH^{-} amount to an excess of alkaline reactant of approximately 30%. 0.5 M sodium hydroxide (NaOH) solutions, produced in situ by an Electrodialysis with Bipolar Membrane unit (EDBM), were used in all cases. The prototype was washed after each test, while no blockage ever occurred.

Case E1 assessed the $Mg(OH)_2$ precipitation process operating the new prototype following the same injection configuration and operating

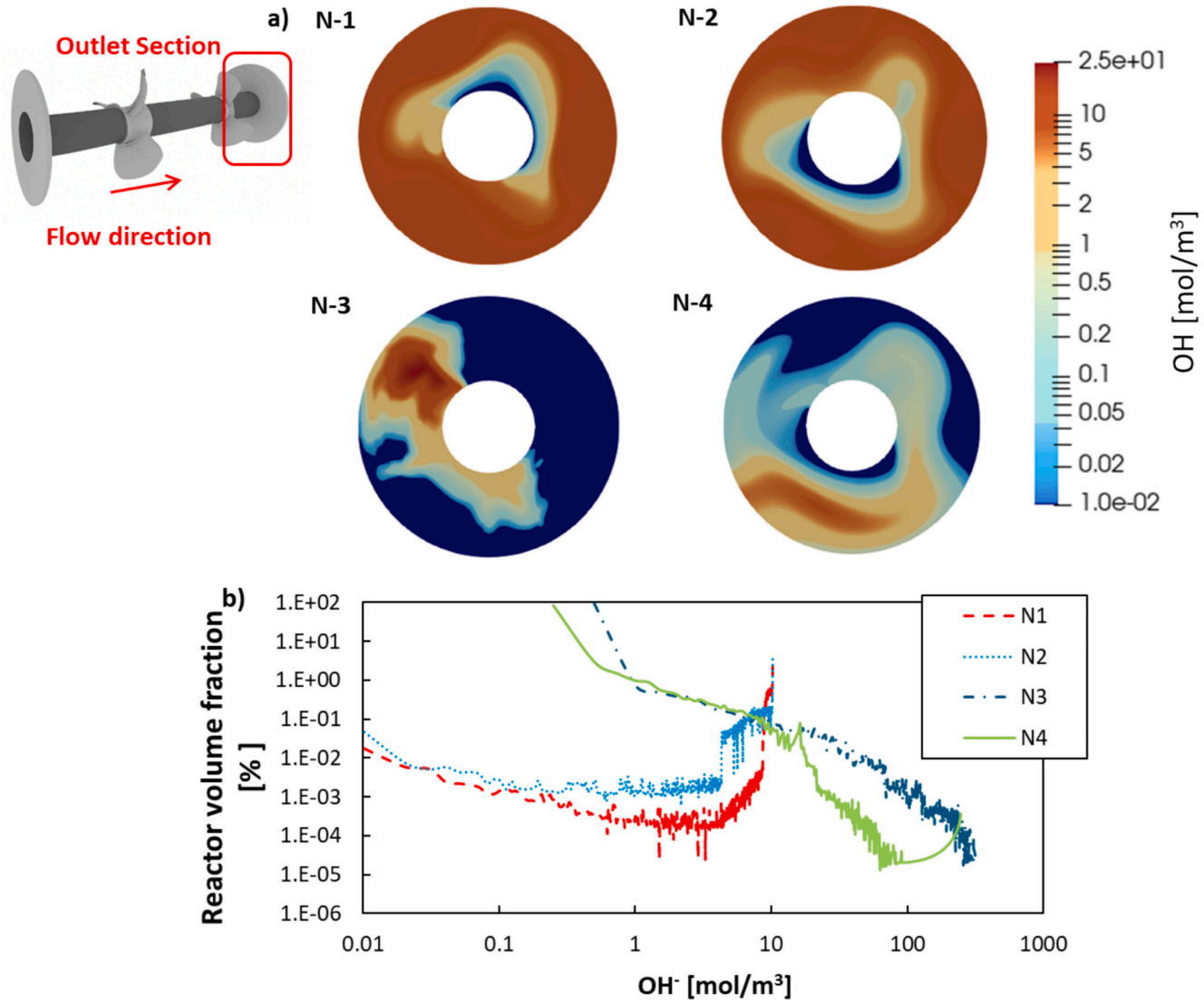

Fig. 4. Concentration maps of OH^- ions at the reactor outlet section (a) and volumetric distribution (no cumulative) of OH^- ion concentration throughout the reactor.

conditions analyzed numerically in Case N1. Case E2 studied the Mg $(OH)_2$ precipitation using Injection configuration 2 with the pre-dilution of reagents, in accordance with Case N4. For completeness, the influence of the pre-dilution of reagents strategy was investigated under Injection configuration 2, see performances of Cases E3 and E4 in the Appendix A. Case E3 corresponds to the non-pre-diluted configuration, consistently with numerical Case N3, whereas Case E4 corresponds to the N4 configuration as Case E2, but employing a different bittern in terms of ionic composition. Thus, E2 and E4 are both associated with the numerical Case N4. Although not discussed in detail here for brevity, this supplementary analysis provides further evidence supporting the reliability of the proposed numerical model.

An additional Case (E2-SYN) was also analyzed feeding the reactor with synthetic $MgCl_2$ and NaOH solutions to investigate the possible influence of ions on settling and filtration rates of $Mg(OH)_2$ suspensions, resulting in negligible differences between the rates obtained with real and synthetic solutions (see Section S2 in the Supporting Information).

4.3. Analytical procedure and performance parameters

Mg(OH)2 suspensions and powders were characterized as reported in Fig. 8.

In each test, 500 mL of $Mg(OH)_2$ suspension was collected at the outlet of the prototype in a graduated glass cylinder and other 100 mL was withdrawn for particle size distribution assessment. Before each sampling, the crystallizer was operated until a steady-state condition was attained. Approximately a period of about 4–5 residence times was waited (30–50 min depending on the operating conditions). The steady-state operation was further verified by monitoring the outlet pH and electrical conductivity of the suspension. A certain amount of the 100 mL suspension was added to a beaker filled with 700 mL of distilled water aiming at reaching a suspension concentration of about ~0.15 g/L. Suspensions were analyzed by the Malvern® Mastersizer 2000 (point 1^I in Fig. 8) before and after applying an ultrasound treatment of 5 min and adding 30 drops of the dispersant poly(acrylic acid, sodium salt), (PAA, MW 1200, Sigma-Aldrich, Inc.). The same PSDs assessment procedure adopted by Battaglia et al. [7] was followed. Sedimentation of the suspensions filled in the 500 mL cylinder was recorded over 24 h (point 1 in Fig. 8). The initial settling velocity was then determined by calculating the slope of the settling curve between the 2nd and 20th minute, using a height [mm] versus time [h] plot, as also discussed by Ventimiglia et al. [31]. After settling, the clarified solution was analyzed and the residual Mg^{2+} content assessed via complexometric titration (point 2 in Fig. 8) using Ethylenediaminetetraacetic acid (EDTA,

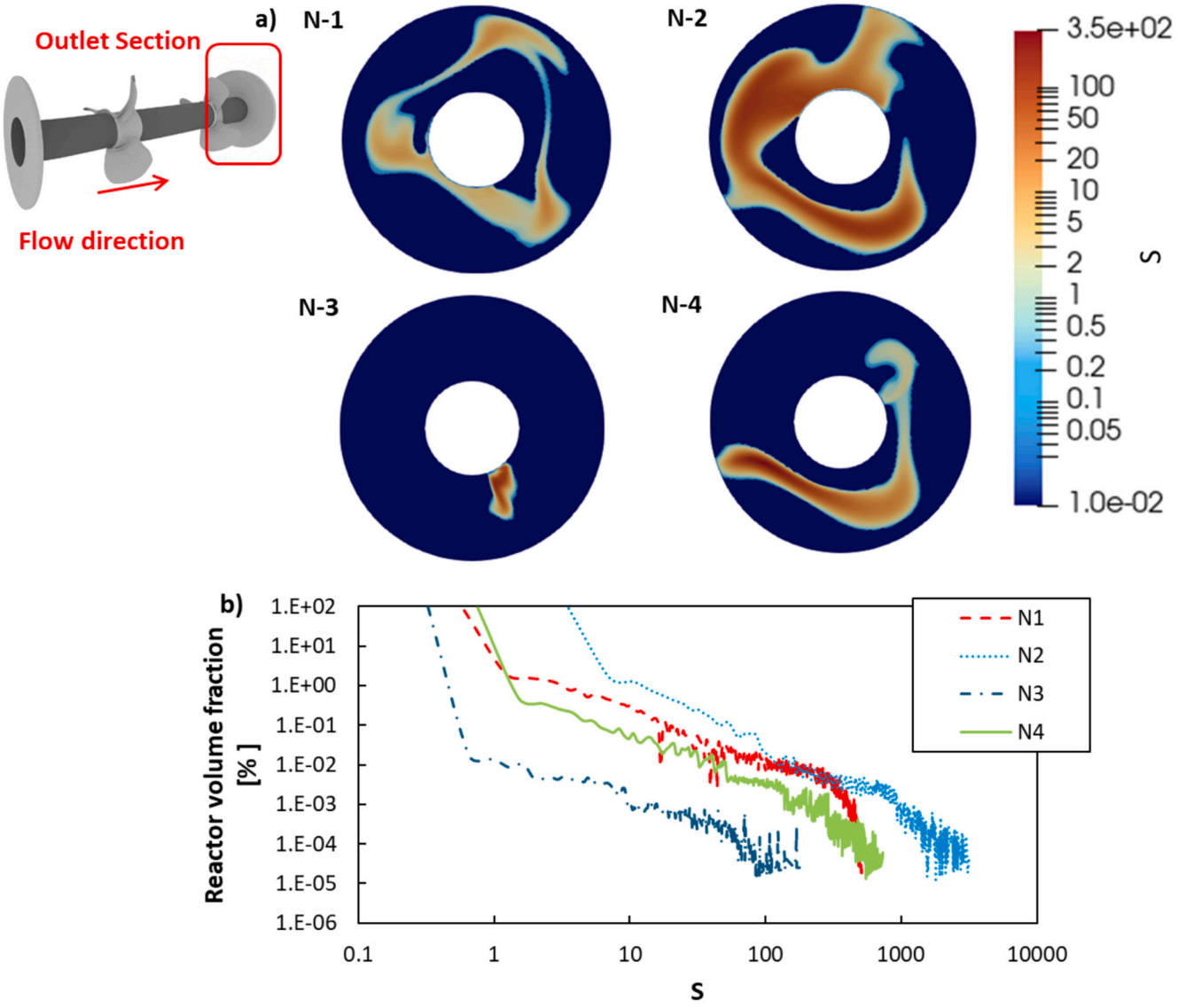

Fig. 5. Spatial distribution maps of supersaturation (S) at the reactor outlet section (a) and volumetric distribution (no cumulative) of S throughout the reactor.

Honeywell | FlukaTM). Mg2+ recovery was calculated as follows:

$$Mg^{2+}recovery = \frac{Mg^{2+}_{Bittern} - Mg^{2+}_{CLAR} \bullet \left(\frac{Q_{S1}+Q_{S2}}{Q_{S1}}\right)}{Mg^{2+}_{Bittern}} \quad (2)$$

where $Mg^{2+}_{Bittern}$ and Mg^{2+}_{CLAR} are the molar concentration of Mg2+ in the fresh bittern and in the clarified solution after thickening, respectively. Q_{S1} and Q_{S2} are the inlet flow rates of fresh bittern and alkaline solutions, respectively. The $Mg(OH)_2$ suspension was washed with demineralized water, re-suspended by agitation, and left to settle until the conductivity of the supernatant solution was below 200 μS/cm (point 3 in Fig. 8). After washing, a fixed volume of 100 mL of thickened suspension was filtered (point 4 in Fig. 8) in a Buchner funnel using 1.6 μm fiberglass filters (Whatman GF/A grade, GE Healthcare Life Sciences) of 70 mm diameter at an absolute pressure of 0.5 bar, using a vacuum pump (BUCHI, VACUUM V700). Filtration time was recorded and filtration rates were evaluated as:

$$F_{rate} = \frac{V_{sol} \bullet Mg^{2+}recovery[\%] \bullet M_{Mg(OH)_2}}{100 \bullet t_{filt} \bullet A_{filter}} \quad \left[\frac{kg}{m^2 \bullet h}\right] \quad (3)$$

where V_{sol} is the filtered volume of suspension [m^3], A_{filter} is the area of the filter [m^2] and t_{filt} is the filtration time [h]. $M_{Mg(OH)_2}$ is the magma density of the suspension [kg/ m^3], expressed as:

$$M_{Mg(OH)_2} = \frac{Mg^{2+}_{Bittern} \bullet Q_{S1}}{Q_{S1}+Q_{S2}} \frac{\bullet Mg^{2+}recovery[\%]}{100} MW_{Mg(OH)2} \left[\frac{kg}{m^3}\right] \quad (4)$$

where $MW_{Mg(OH)2}$ is the molecular weight of magnesium hydroxide [g/ mol].

The final magma density, $Mf_{Mg(OH)_2}$, was also computed as:

$$Mf_{Mg(OH)_2} = M_{Mg(OH)_2} \bullet \frac{V_f}{V_{in}} \left[\frac{kg}{m^3}\right] \quad (5)$$

where V_f is the final thickened volume [mL] in the cylinder after 24 h and V_{in} is the initial sample volume, typically 500 mL.

Finally, the filtered cake was dried in an oven at 120 °C for 24 h (point 5 in Fig. 8) and the Mg(OH)2 powders were analyzed via scanning electron microscopy technique (SEM, FEI Quanta 200 FEG and JEOL, point 6 in Fig. 8).

4.4. Experimental performance of the novel MFPFR prototype

The MFPFR prototype was designed and operated following the best

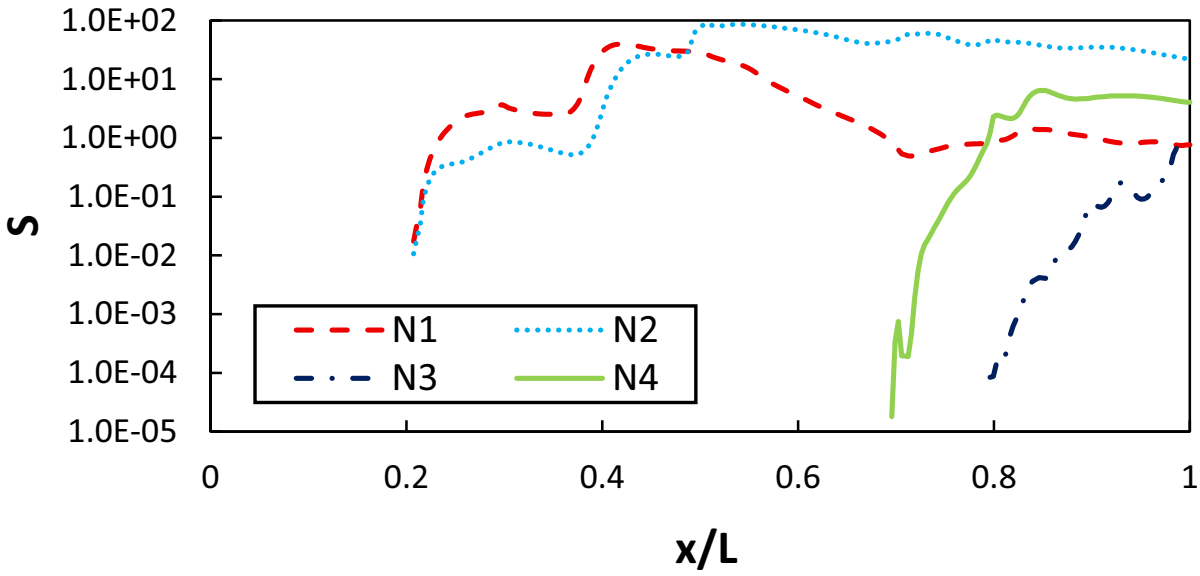

Fig. 6. Axial profiles of the cross-section averaged supersaturation as a function of the normalized reactor length (x/L).

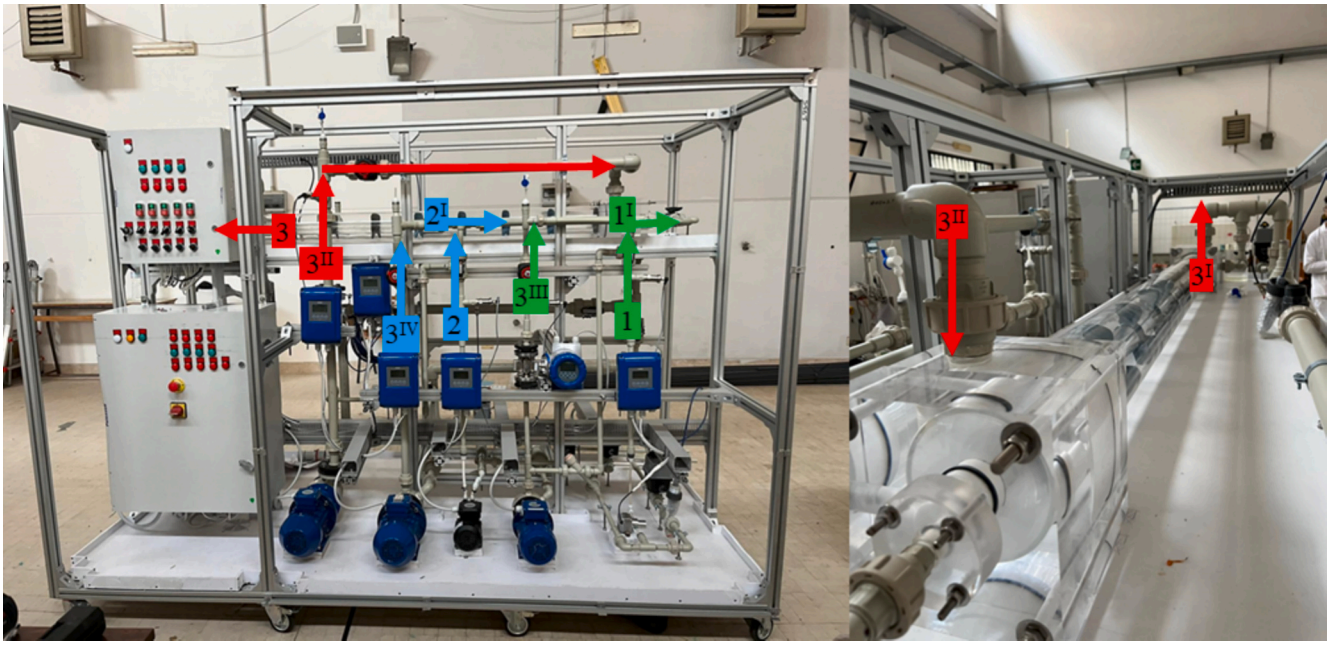

Fig. 7. Pictures of the skid of the MFPFR prototype. Green, blue and red arrows indicate the bittern, the sodium hydroxide solution and the recirculating suspension streams whose nomenclature follows the scheme shown in Fig. 2.

operating conditions selected through the numerical assessment for both Injection configurations 1 and 2, namely Cases N1 and N4. Fig. 9 shows the initial settling velocity (a) and the filtration rate (b) of $Mg(OH)_2$ suspensions produced during tests E1 and E2.

As can be seen in Fig. 9 (a), $Mg(OH)_2$ suspensions exhibited markedly different initial settling velocity values and behaviors when produced in Cases E1 and E2. In Case E1, the settling velocity remained approximately constant at ~140 mm/h within the pH range of 10.2 to 11.2. A further increase in pH led to a sharp decline in velocity, reaching values below 10 mm/h at pH levels above 12, thus indicating a suspension that cannot be effectively separated by sedimentation. Conversely, Case E2 (corresponding to the simulated configuration N4) exhibited a parabolic trend with a distinct maximum. The initial settling velocity was ~130 mm/h for pH values below 10.5, while increasing the pH, the settling velocity reached a peak value of about 440 mm/h in a pH range between 11.5 and 12. This value was almost four times higher than the highest one observed in Case E1. A further increase of pH beyond 12 led to a sharp decline in settling performance. Filtration behavior, Fig. 9 (b), followed settling trends. Specifically, Case E1 exhibited reasonably good filterability performance at pH 10.3 with a filtration rate of 37 kg/(m^2·h). Performance decreased to approximately 12.4 kg/(m^2·h) (one-third) at pH 11.1. At higher pH values, the suspension became physically unfilterable (data points not reported in the graph). In Case E2, at low pH values, filtration rates were comparable to those of Case E1, while increasing the pH value a sharp increase was observed reaching values between 70 and 85 kg/(m^2·h) in the pH range between 11.5 and 12.0. At pH values above 12, the filtration rate dropped again to around 10 kg/(m^2·h).

Table 2
Ionic composition of bitterns adopted in the experimental campaign. The Limit of Quantification (LOQ) for Ca ions is 0.002 g/L.

Macro-component	Bittern [g/L]	Bittern [mol/L]	Analytical technique
Na^+	41 ± 1	1.80 ± 0.04	IC*
K^+	14.9 ± 0.5	0.38 ± 0.01	IC*
Mg^{2+}	50 ± 1	2.06 ± 0.04	IC*/EDTA**
Cl^-	148 ± 5	4.18 ± 0.14	IC*
SO_4^{2-}	56 ± 1	0.59 ± 0.01	IC*

Micro-component	Bittern [mg/L]	Bittern [mol/L]	Analytical technique
Ca^{2+}	<LOQ	<LOQ	IC*/EDTA**
B	125 ± 1	0.0116 ± 0.0001	ICP-OES***

* Ion Chromatography (IC).
** Complexometric titration with EDTA.
*** Inductively Coupled Plasma Optical Emission Spectroscopy (ICP-OES).

These results acquire particular significance when interpreted in the light of the supersaturation regimes discussed earlier. Battaglia et al. [39], working with concentrated saltwork bitterns (Mg^{2+} 2 M) similar to those described by Alamdari et al. [15], operated a pilot-scale reactor at pH 10.8 and 12.8. The resulting suspensions had initial magma density of 13.2 and 8.5 g/L and exhibited filtration rates of 8.6 and 1.3 kg/(m^2·h), respectively. In addition, an initial settling velocity could not be reliably determined because sedimentation was extremely slow in both cases, reaching its conclusion only after ~3000 min. By contrast, Ventimiglia et al. [31] and Turek et al. [10] investigated the use of dilute solutions, comparable to those studied by Yuan et al. [14]. Ventimiglia et al. [31], operating a reactor with desalination brine containing ~2 g/L of Mg^{2+} and 0.5 M NaOH, explored reaction pH of 10.0, 11.2, and 12.4. The initial magma densities of suspensions were 2.5, 3.4, and 3.2 g/L, while settling velocities reached 274, 417, and 39 mm/h, with corresponding filtration rates of 2.6, 6.5, and 1.9 kg/(m^2·h), respectively. Turek et al. [10] precipitated $Mg(OH)_2$ from mine brine containing 2.84 g/L of Mg^{2+} (~0.117 M) under stoichiometric NaOH dosing. Although magma density was not reported (it is expected to be very low given the dilute feed), they achieved settling velocities of 70–170 mm/h and filtration rates of 3–9 kg/(m^2·h), depending on agitation intensity and temperature. Remarkably, the present study delivers settling velocities up to 440 mm/h and filtration rates above 80 kg/(m^2·h), translating into roughly one to two orders of magnitude higher solid/liquid separation performance than the bittern reference case. Even when compared with dilute brine studies, the results remain clearly superior, with settling at least comparable to the best reported values and filtration still exceeding literature performance by more than an order of magnitude.

A possible explanation behind settling and filtration behaviors can lay on the combined effect of local supersaturation, local hydrodynamics (affected by the use of the different injection *configuration*) in the reactor and the influence of electrostatic interactions (such as lyosorption and zeta-potential of particles) between particles at different pH values. In details:

- The injection of the reactants in Case E1 emulated a single-feed system, as discussed in section 3, where the bittern is injected into a basic environment. This promotes an instantaneous contact between reagents that can cause high local supersaturation levels. Note that, increasing the flow rate of the NaOH solution to enhance the pH value induced a higher local concentration of hydroxyl ions and thus supersaturation (assuming constant micromixing efficiency). Conversely, in case E2, the employed injection–dilution–reaction strategy effectively allows to control and reduce supersaturation in the reactor volume, as suggested by numerical results. This is further evident when comparing the performance of the prototype with and without the use of the pre-dilution strategy of the reactants. As reported in Appendix A, the pre-dilution of the reagents (Case E4) had a significant impact on $Mg(OH)_2$ suspension characteristics, with a twofold improvement in both settling and filtration rates with respect to the non-pre-dilution case (Case E3), indicating a better control of the local mixing and supersaturation conditions in accordance with numerical results of Cases N3 and N4. It is worth recalling that, as discussed in section 3.3, the pre-dilution of the reagents can also have a detrimental effect depending on the adopted injection system as observed for Cases N1 and N2. In this latter case, the high local micro mixing condition promoted by the pre-dilution strategy (Case N2) caused higher supersaturation values than those calculated in the non-prediluted N1 case.
- Zeta potential is a key parameter governing interaction between colloidal particles in a suspension, since it represents the electrostatic potential at the slipping plane of particles dispersed in a liquid. When the absolute value of zeta potential is high (>30 mV), electrostatic repulsion hinders particle–particle attachment. Conversely, when the zeta potential approaches zero (isoelectric point), electrostatic interactions are minimized and aggregation becomes more favorable [40]. Literature data indicate that $Mg(OH)_2$ particles reach their isoelectric region in the alkaline pH range between 11 and 12 [7,41–44]. However, although zeta potential can indicate whether aggregation is favored or not, the effectiveness of aggregation also depends on the size and morphology of crystals/particles, the latter phenomena also strongly affected by the local supersaturation regime, as discussed above.
- Lyosorption is the formation of lyospheres, namely aggregated structures that entrap large volumes of solvent, that results in isodense particles with scarce settling performance. This phenomenon is promoted at high pH values (>12.5) [10,31].

Overall, it can be postulated that, in Case E1 supersaturation and lyosorption were the dominant factors overcoming the zeta-potential of particles. As the pH increased, both effects intensified, leading to the formation of very fine, solvent-rich particles that exhibited scares settling and filtration properties, see Fig. 9 **(a)**.

On the other hand, in Case E2, the use of the pre-dilution as well as the novel Injection configuration 2 strategy reduced local supersaturation values leading to a possible observation of the influence of the zeta potential on precipitated particles. As a matter of fact, increasing the pH led to a parabolic trend of filtration and settling performance of the suspensions reaching the best condition at the isoelectric point, as observed in Fig. 9 (b**)**. A further increase of the pH makes lysorption and local supersaturation levels dominant phenomena, hindering suspension performance.

The influence of these phenomena as function of pH values for Cases E1 and E2 can be further studied in SEM images shown in Fig. 10.

In Case E1, $Mg(OH)_2$ powders exhibited a moderate degree of crystallinity at a low pH of 10.6. Primary crystals with a hexagonal morphology were formed alongside amorphous ones (Fig. 10, a1 and a2). An increase of the pH to a value of 11.2 resulted in a complete decline in crystallinity, yielding amorphous aggregates in which the hexagonal crystals were replaced by completely irregular entities (Fig. 10, b1 and b2), due to the prevailing effect of high supersaturation levels.

In Case E2, similar results were obtained at low pH values, as well as for other parameters previously analyzed, emphasizing the minimal difference in terms of morphology between the two configurations at this operating point. At pH 11.9, close to the $Mg(OH)_2$ particles isoelectric point, highly aggregated particles with a very high degree of crystallinity were observed. Specifically, hexagonal platelets formed with the complete disappearance of amorphous zones in the solid (Fig. 10, d1 and d2). This phenomenon was attributed to the enhanced ion diffusion mechanism around the crystal under zero zeta potential

Table 3
Summary of operating conditions adopted in the experimental campaign: injection configuration, Mg^{2+} solution flow rates and concentrations before and after pre-dilution (S.1 and S·1^{I}), OH^{-} solution flow rates and concentrations before and after pre-dilution (S.2 and S·2^{I}). In all tests, the main recirculating 3^{IV} stream was fixed at 130 L/min. Note that, in the Injection configuration 1, the recirculating 3^{IV} stream corresponds to the S·2^{I}. In addition, the adopted pumps had a ± 5% flow rate oscillation with respect to their set point. Mg^{2+} and OH^{-} concentrations in streams S·1^{I} and S·2^{I} were calculated based on mass balance calculations.

Cases	Inj. conf.	S.1 [L/min]	S.1^{I} [L/min]	Mg^{2+} conc. (S.1) [M]	Mg^{2+} conc. (S·1^{I}) [M]	S.2 [L/min]	S·2^{I} [L/min]	OH^{-} conc. (S.2) [M]	OH^{-} conc. (S·2^{I}) [M]
E1	1	0.33	0.33	2.06 ±0.04	2.06	2.70, 2.85, 3.06, 3.20, 3.50	130	0.50 ±0.02	0.010, 0.011, 0.012, 0.012, 0.013
E2	2	0.33	5.33	2.06 ±0.04	0.125	2.65, 2.70, 2.85, 3.06, 3.20, 3.50, 3.70	5.33	0.50 ±0.02	0.250, 0.253, 0.267, 0.287, 0.300, 0.328, 0.347

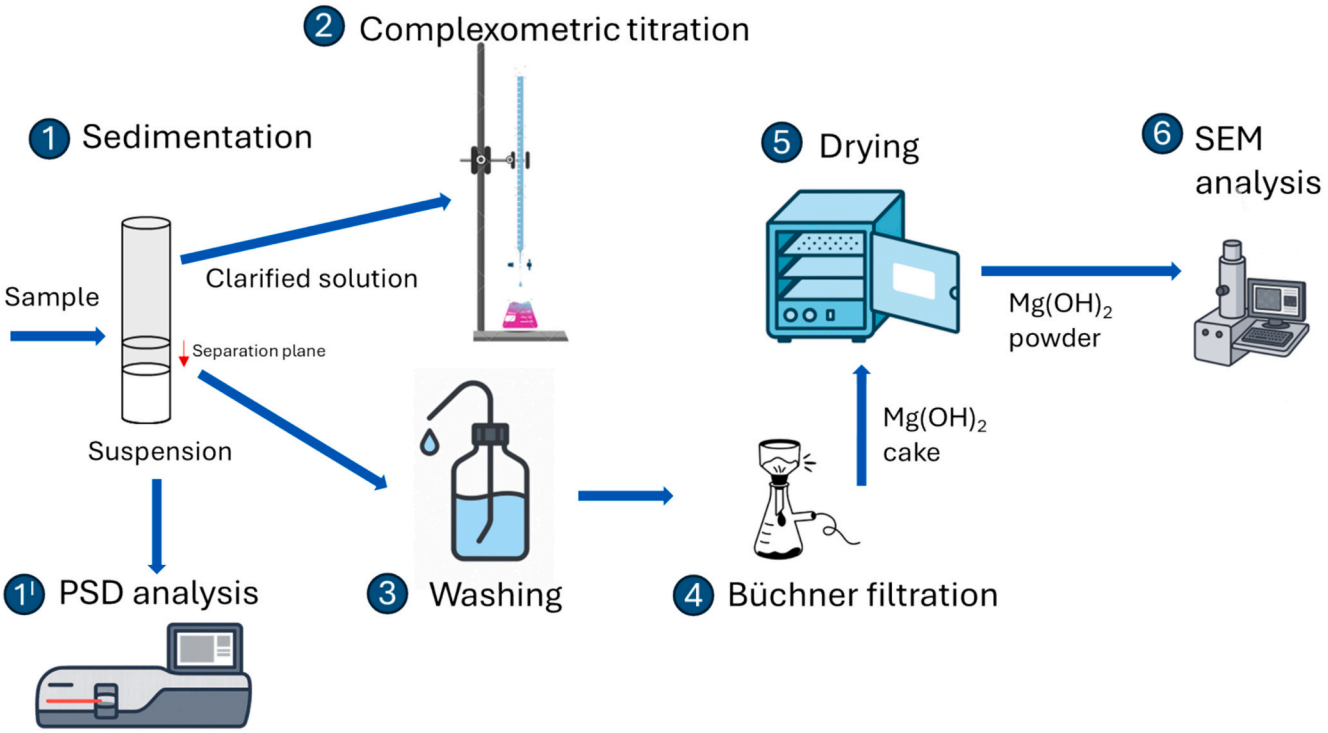

Fig. 8. Analytical processing of $Mg(OH)_2$ suspensions and powders.

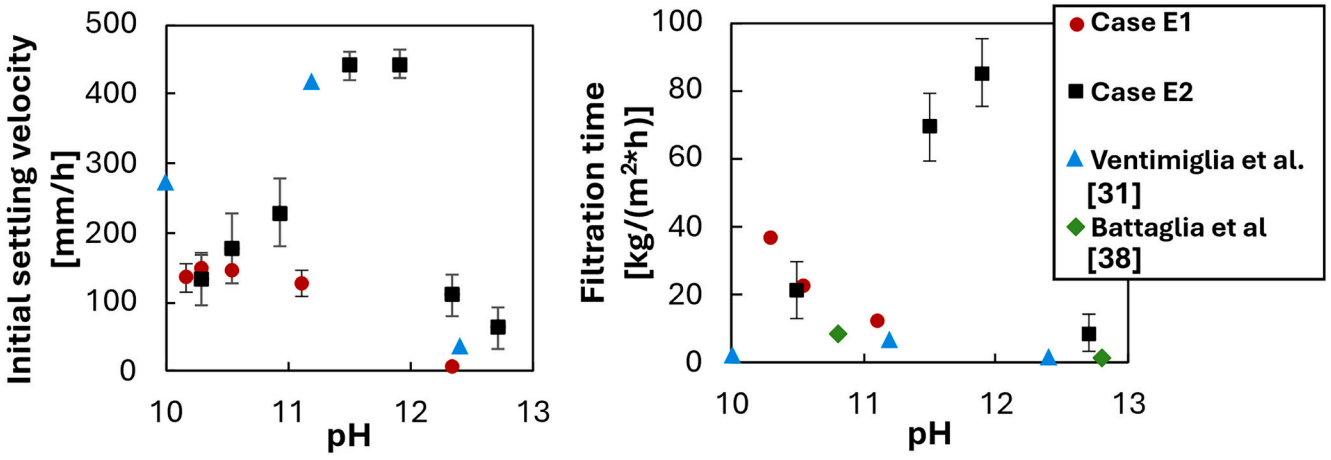

Fig. 9. Initial settling velocity values (a) and filtration rates (b) for Cases E1 (red dots) and E2 (black squares). For the sake of comparison, the blue triangles and the green circles represent the values reported by Ventimiglia et al. [31] and Battaglia et al. [38], respectively.

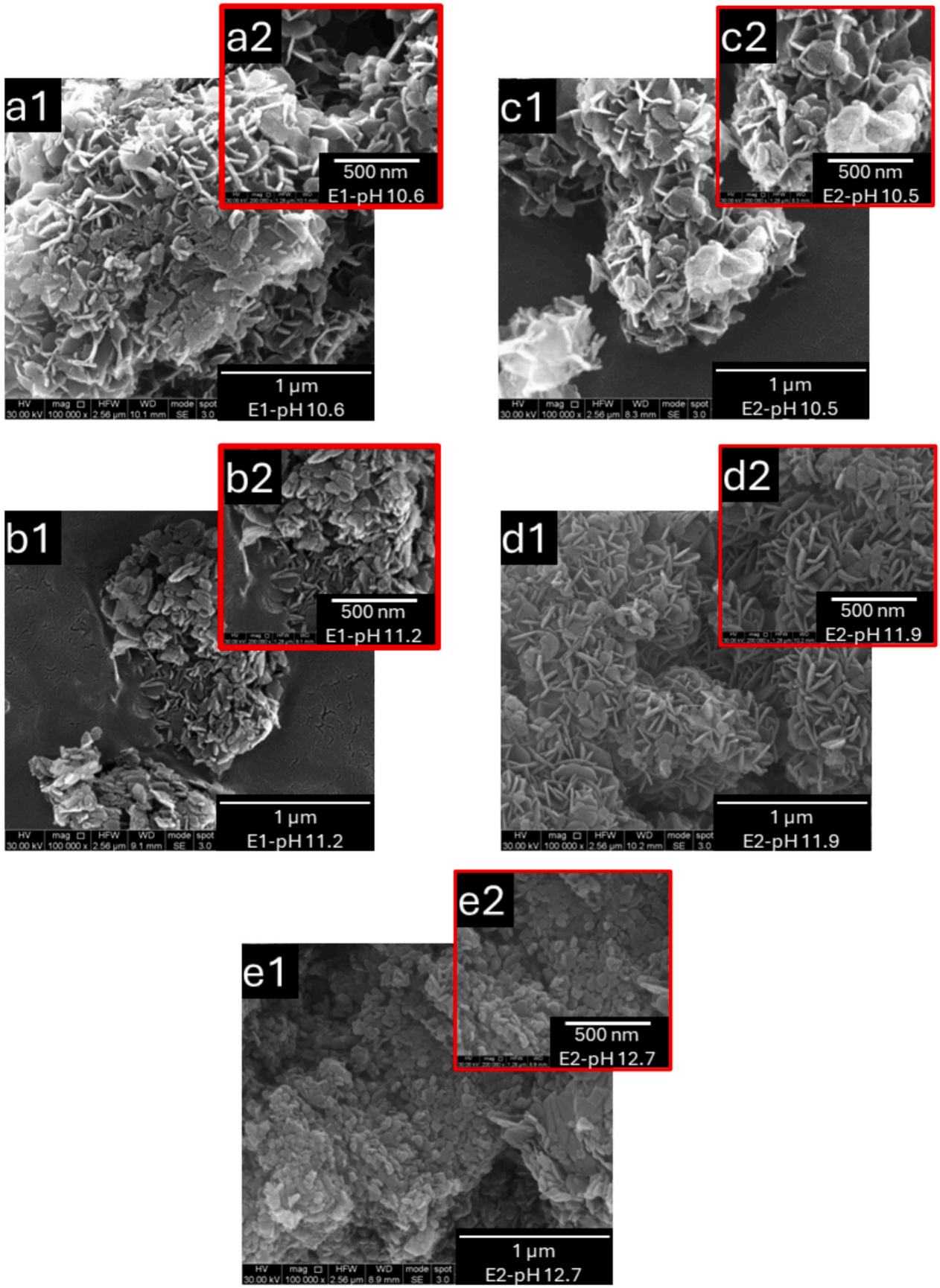

Fig. 10. *SEM images of $Mg(OH)_2$ powders for Case E1 at pH 10.6 (a1, a2) and pH 11.2 (b1, b2), and for Case E2 at pH 10.5 (c1, c2), pH 11.9 (d1, d2), and pH 12.7 (e1, e2), shown at magnifications of 100,000× and 200,000 × .*

Table 4
Initial magma density, final magma density after the thickening process and Mg^{2+} recovery in Case E1.

pH	Initial Magma density [g/L]	Magma density after thickening [g/L]	Mg^{2+} recovery
10.2	10.6 ± 0.2	45.8 ± 0.9	81.6 ± 0.1
10.3	11.2 ± 0.2	48.2 ± 1.0	90.2 ± 0.1
10.5	11.0 ± 0.2	47.5 ± 1.0	94.8 ± 0.1
11.1	11.0 ± 0.2	47.5 ± 1.0	98.6 ± 0.1
12.4	10.4 ± 0.2	44.3 ± 0.9	99.7 ± 0.1

Table 5
Initial magma density, final magma density after the thickening process and Mg^{2+} recovery in Case E2.

pH	Initial Magma density [g/L]	Magma density after thickening [g/L]	Mg^{2+} recovery
10.3	11.0 ± 0.2	31.4 ± 0.6	82.39 ± 0.1
10.6	12.1 ± 0.2	38.8 ± 0.8	92.29 ± 0.1
10.9	12.2 ± 0.2	41.2 ± 0.8	97.95 ± 0.1
11.5	11.7 ± 0.2	146.4 ± 2.8	99.74 ± 0.1
11.9	11.2 ± 0.2	112.2 ± 2.2	>99.90
12.4	10.3 ± 0.2	79.5 ± 1.5	>99.90
12.7	9.8 ± 0.2	65.2 ± 1.3	>99.90

conditions [45]. The resulting hexagonal platelets had the best filtration and settling properties. Upon further increasing the pH to 12.7, the system underwent a complete loss of crystalline order, giving rise to poorly defined, submicron-sized globular particles (Fig. 10, e1 and e2). In this latter case, the resulting highly porous and nested structures accounted for the severe challenges encountered in the separation processes previously discussed, where lyosorption was deemed to be the most influencing phenomenon on separation performance.

As discussed so far, local supersaturation, local hydrodynamics and electrostatic interactions (such as lyosorption and zeta-potential of particles) between particles at different pH values strongly affect particle morphology, settling and filtration rates. A possible influence of the above phenomena on particle size distributions of $Mg(OH)_2$ particles was also investigated. Results are reported and discussed in section S3 in the Supporting Information. PSDs ranged between 1 and 10 μm, after the ultrasound and PAA treatment, regardless of operating conditions and reactor configurations. This was mainly attributed to the strong aggregation phenomena occurring in the MFPFR reactor induced using the recirculation strategy that enhances collisions between particles through their circulation in the reactor volume, as also discussed in Morgante et al. [46].

Overall, experimental observations were consistent with the numerical predictions of supersaturation and reagent distribution within the reactor volume across Cases N1 to N4. Supersaturation profiles derived from simulations under stoichiometric conditions indicated Configuration N4 (E2) as the most effective in controlling local supersaturation. This prediction was confirmed by the best settling, filtration and produced $Mg(OH)_2$ particles (in terms of morphology), thereby validating the numerical approach and establishing Configuration N4 as the reference configuration for further possible reactor optimization.

For the sake of completeness, Table 4 and Table 5 report the values of initial magma density (Eq. 4), final magma density (Eq. 5) at the end of the thickening process, and magnesium ion recovery (Eq. 2) for Cases E1 and E2, respectively. These numbers are useful for a fair comparison of settling and filtration performance of $Mg(OH)_2$ slurries.

In Case E1, the magma density increased approximately fourfold, from an initial value of ~10 g/L to around 50 g/L, regardless of the reaction pH, after the settling process. It is also noteworthy that magnesium ion recovery exceeded 98% at pH values above 11.0, while under near-stoichiometric conditions, the recovery reached only about 80%. A trend with a maximum in the final magma density values was observed for Case E2, Table 5, in accordance with thickening and filtration results. Peaks of ~150 g/L and ~ 110 g/L were achieved at pH value of 11.5 to 11.9, corresponding to a concentration factor of ~13 and ~ 10. In agreement with Case E1, the magnesium conversion in Case E2 also exceeded 98% at pH values above 11.0.

5. Conclusions

This study presented a model-based strategy for design optimization of a crystallizer dedicated to the recovery of magnesium hydroxide from concentrated saline solutions. CFD simulations were employed to compare alternative reactor configurations with the goal of mitigating local supersaturation, the key parameter governing crystallization phenomena. The influence of injection configurations of the reagents and pre-dilution strategies, before reagents injection through nozzles and in the reaction environment by $Mg(OH)_2$ recirculation streams, were investigated. Among the simulated cases, Injection configuration 2 with pre-dilution of reactants (Case N4) emerged as the most effective option, providing reduced supersaturation peaks and more homogeneous reagent distribution.

Specifically, the injection configuration 1 resembled a single-feed system, in which the bittern was injected into the annular section of the reactor, through nozzles, where OH^- species were already well diluted through the recirculation of produced $Mg(OH)_2$ suspension fed to the annular region of the reactor (Cases N1 and N2). In contrast, in the Injection configuration 2 (N2 and N4 cases) strategy, both the NaOH and bittern solutions were injected separately, as in a double-feed reactor. In this latter case, the injection configuration and the pre-dilution of reactants avoided the direct contact of highly concentrated reagents, thus controlling local micromixing and supersaturation levels. On the other hand, the pre-dilution of reagents before their injection (case N2) had a detrimental effect when adopting the injection system 1, where the higher flow rates caused higher local micro mixing enhancing supersaturation with respect to the non-prediluted case (N1).

The numerical findings were translated into a pilot-scale prototype, which was constructed and operated under real process conditions. Experimental campaigns confirmed the predictive outcomes of the simulations, despite crystallization phenomena and population balance equations were not computed in simulations: when operated according to the N4 configuration, the reactor delivered markedly improved solid–liquid separation, with settling velocities up to 440 mm/h and filtration rates exceeding 80 kg/(m^2·h) within the optimal pH range of 11.5–12.0. SEM analyses further demonstrated that these conditions promoted the formation of highly crystalline hexagonal platelets, whereas less favorable regimes led to amorphous or globular morphologies. In addition, comparison between Cases E3 and E4 clearly highlighted the beneficial effect of the pre-dilution strategy of the reactants when adopting the injection system 2, observing a twofold improvement in both settling velocity and filtration rate of $Mg(OH)_2$ suspensions passing from a non-prediluted condition to a prediluted one.

The strong agreement between numerical predictions and experimental evidence highlights the potential of CFD-guided design for crystallizer optimization. This approach not only allowed the identification of the best-performing configuration but also accelerated the transition from conceptual design to pilot-scale validation.

In summary, the adoption of Injection configuration 2 with pre-dilution as the reference configuration provides a robust foundation for further optimization and scale-up of MFPFR technology. The outcomes of this work directly support the development of the 100 t/y demonstration plant within the MareMag LIFE project, representing a significant step toward the industrial valorization of saline effluents into high-quality magnesium hydroxide.

Nomenclature and abbreviations

MDH	magnesium dihydroxide
S	supersaturation
CFD	computational fluid dynamics
PBE	population balance equations
PSD	particle size distribution
MFPFR	Multiple Feed Plug Flow Reactor
k	turbolent kinetic energy [m^2/s^2]
ω	specific dissipation rate [1/s]
u	velocity [m/s]
P	pressure [Pa]
C	chemical species concentration [mol/m^3]
F_{rate}	filtration rate [$kg/(m^2 \cdot h)$]
$M_{Mg(OH)2}$	magma density of magnesium hydroxide [g/L] or [kg/m^3]
$M_{FMg(OH)2}$	final magma density of magnesium hydroxide [g/L] or [kg/m^3]
V_f	final volume [mL]
MW	molecular weight [g/mol]
SEM	scanning electron microscope
LOQ	limit of quantification

CRediT authorship contribution statement

Ferdinando Miciletta: Writing – original draft, Visualization, Validation, Software, Methodology, Investigation, Formal analysis, Data curation, Conceptualization. **Giuseppe Battaglia:** Writing – original draft, Visualization, Validation, Supervision, Methodology, Investigation, Formal analysis, Data curation, Conceptualization. **Fabrizio Vicari:** Writing – review & editing, Visualization, Supervision, Resources, Project administration, Methodology, Funding acquisition, Conceptualization. **Fabrizio Vassallo:** Visualization, Methodology, Conceptualization. **Daniele Marchisio:** Writing – review & editing, Visualization, Supervision, Methodology. **Alessandro Tamburini:** Writing – review & editing, Visualization, Supervision, Resources, Project administration, Methodology, Funding acquisition, Conceptualization. **Andrea Cipollina:** Writing – review & editing, Visualization, Supervision, Resources, Project administration, Methodology, Funding acquisition, Conceptualization. **Giorgio Micale:** Writing – review & editing, Visualization, Supervision, Resources, Project administration, Methodology, Funding acquisition, Conceptualization.

Declaration of competing interest

Authors Vicari and Vassallo are employees of ResourSEAs, the company owing the technological IP for commercialization of the reactor described in this work.

Acknowledgement

This work has received funding from the European Union's LIFE 2021-2027 programme under Grant Agreement 101147407 - LIFE23-ENV-IT-MAREMAG LIFE. Views and opinions expressed are however those of the author(s) only and do not necessarily reflect those of the European Union or CINEA. Neither the European Union nor CINEA can be held responsible for them.

This work was supported by the EU within SEArcularMINE (Circular Processing of Seawater Brines from Saltworks for Recovery of Valuable Raw Materials) project – Horizon 2020 programme, Grant Agreement No. 869467. This output reflects only the author's view. The European Health and Digital Executive Agency (HaDEA) and the European Commission cannot be held responsible for any use that may be made of the information contained therein.

The authors are grateful to Daniele Milia, Francesco Volpe and Damiano Costanzino for their support to the pilot construction and some CFD simulations.

Appendix A. Influence of the pre-dilution strategy

To further validate the numerical campaign, the influence of the pre-dilution strategy of reagents via $Mg(OH)_2$ suspension recirculation was investigated adopting the Injection configuration 2 at a fixed pH of 12 (near-complete conversion of magnesium ions and good $Mg(OH)_2$ performances, based on experimental).

In the tests, due to the lack of the bittern of tests E1 and E2, another bittern was collected from Trapani saltworks. Note that, due to sampling location and month variability, the bittern had a slightly different composition than that reported in Table 2. The composition of the 2nd bittern is reported in Table A1.

Table A1
Ionic composition of the bittern adopted in the experimental campaign to assess the influence of pre-dilution strategy. The same analytical procedure described in the main text was employed for the characterization of the solution. The Limit of Quantification (LOQ) for Ca ions is 0.002 g/L.

Macro-component	Bittern 2 [g/L]	Bittern 2 [mol/L]	Analytical technique
Na^+	64 ± 1	2.80 ± 0.04	IC*
K^+	6.7 ± 0.3	0.17 ± 0.01	IC*
Mg^{2+}	39 ± 1	1.60 ± 0.04	IC*/EDTA**
Cl^-	194 ± 5	5.47 ± 0.14	IC*
SO_4^{2-}	34 ± 1	0.35 ± 0.01	IC*

Micro-component	Bittern [mg/L]	Bittern [mol/L]	Analytical technique
Ca^{2+}	<LOQ	<LOQ	IC*/EDTA**
B	125 ± 1	0.0116 ± 0.0001	ICP-OES***

* Ion Chromatography (IC).
** Complexometric titration with EDTA.
*** Inductively Coupled Plasma Optical Emission Spectroscopy (ICP-OES).

Table A2 lists details of the operating conditions adopted to study the influence of the reagents pre-dilution strategy. The same experimental and analytical procedures described in the main text were followed for the characterization of $Mg(OH)_2$ suspensions and powders.

Table A2
Operating conditions to study the influence of the pre-dilution strategy: Mg^{2+} solution flow rates and concentrations before and after pre-dilution (S.1 and $S.1^{I}$), OH^{-} solution flow rates and concentrations before and after pre-dilution (S.2 and $S{\cdot}2^{I}$). In all tests, the Injection configuration 2 was chosen and the recirculating 3^{IV} stream was always fixed at 130 L/min. The adopted pumps had a ± 5% flow rate oscillation with respect to their set point. Mg^{2+} and OH^{-} concentrations in streams $S.1^{I}$ and $S.2^{I}$ were calculated based on mass balance calculations.

Cases	S. 1 [L/min]	S. 1^{I} [L/min]	Mg^{2+} conc. (S.1) [M]	Mg^{2+} conc. ($S{\cdot}1^{I}$) [M]	S.2 [L/min]	S. 2^{I} [L/min]	OH^{-} conc. (S.2) [M]	OH^{-} conc. ($S{\cdot}2^{I}$) [M]
E3	0.33	0.33	1.60 ±0.04	1.60	2.65	2.65	0.50 ±0.02	0.50
E4	0.33	5.33	1.60 ±0.04	0.100	2.65	5.33	0.50 ±0.02	0.25

The operating conditions were selected to resemble those numerically analyzed in Cases N3 and N4. The same operating conditions of case E2 were used in E4, where the main difference was the adopted bittern.

Fig. 11 shows the initial settling velocity (a) and filtration rate (b) of $Mg(OH)_2$ suspensions synthesized in tests E3 and E4.

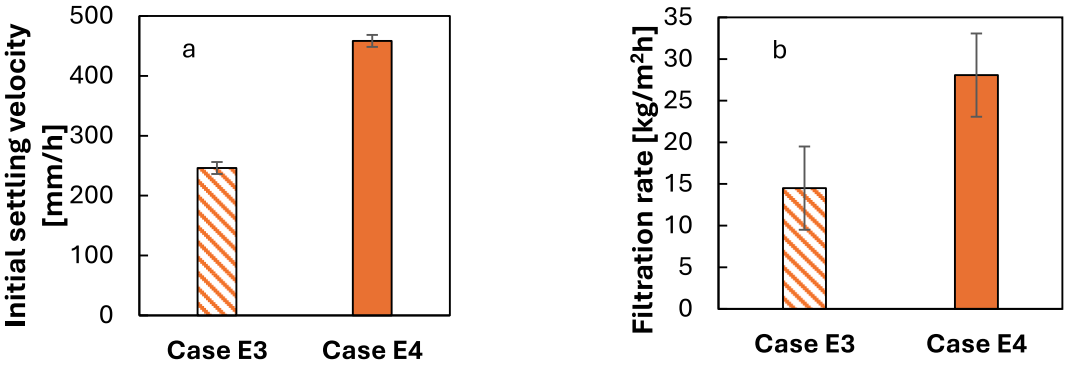

Fig. 11. (a) Initial settling velocity and (b) filtration rate for Cases E3 (hatched bar) and E4 (solid bar).

The pre-dilution of the reagents had a significant impact on $Mg(OH)_2$ suspension characteristics with a twofold improvement in both settling velocity and filtration rate for Case E4 compared to Case E3. Specifically, suspensions produced in Cases E3 and E4 exhibited initial settling velocities of 246 mm/h and 458 mm/h, and filtration rates of 15 kg/(m^2·h) and 30 kg/(m^2·h), respectively. Results confirm the outcomes provided by numerical assessment. The poor macromixing level in Case N3 (conditions similar to E3) would cause precipitation process to occur under uncontrolled conditions that, although better than Case E1, would hinder the performance of $Mg(OH)_2$ slurries. Fig. 12 reports SEM images of $Mg(OH)_2$ powders obtained at pH 12.0 in Cases E3 (a1 and a2) and E4 (b1 and b2).

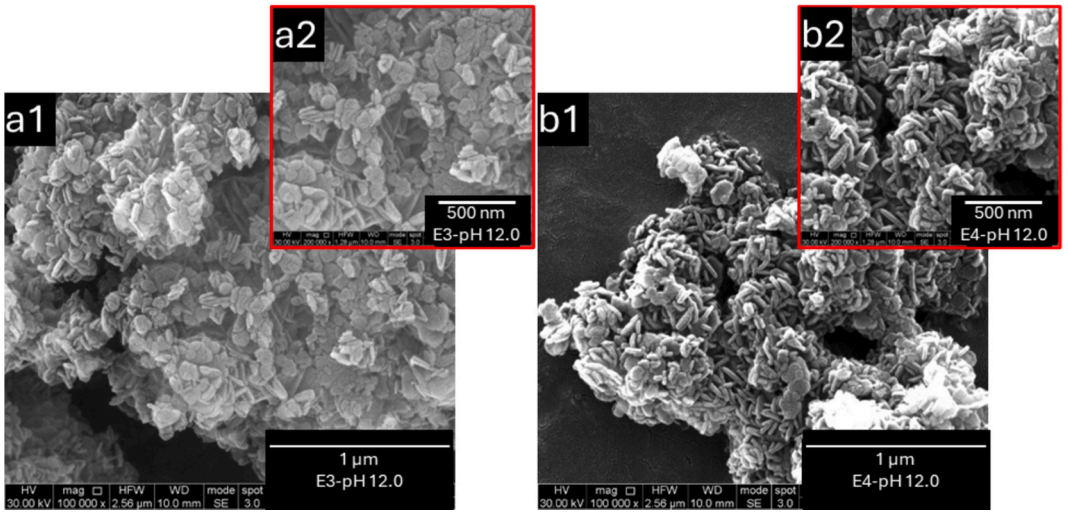

Fig. 12. SEM images of $Mg(OH)_2$ powders produced in Case E3 (a1, a2) and E4 (b1, b2) at a magnification of 100,000× and 200,000× at pH 12.

The SEM images shown in Fig. 12 clearly demonstrate that aggregated particles were formed in both cases. Powders in Case E4 exhibited a higher degree of crystallinity, featuring hexagonal platelet-shaped crystals with a more pronounced thickness, thanks to the better reactant distribution in the reactor volume.

Table 6 reports values of initial magma density (Eq. 4), final magma density after thickening (Eq. 5) and Mg^{2+} recovery (Eq. 2) of the suspensions produced in tests E3 and E4.

Table 6
Initial magma density, final magma density after the thickening process and Mg^{2+} recovery in Case E1.

Case	Initial Magma density [g/L]	Magma density after thickening [g/L]	Mg^{2+} recovery [%]
E3	10.3 ± 0.2	129.1 ± 2.5	>99.90
E4	10.3 ± 0.2	172.1 ± 3.3	>99.90

$Mg(OH)_2$ suspensions produced in Case E4 reached a value of 172 g/L after 24 h of thickening, achieving a thickening degree approximately 30% higher than Case E3. Mg^{2+} recovery was always greater than 99% due to the adopted pH value of 12, confirming the absence of influence from other types of operating conditions.

Appendix B. Supplementary data

Supplementary data to this article can be found online at https://doi.org/10.1016/j.cej.2026.177992.

Data availability

Data will be made available on request.

References

[1] M.D. Walter, M.T. Wajer, Overview of Flame Retardants Including Magnesium Hydroxide. https://magnesiaspecialties.com/technical-resources/MagShield-Overview-of-Flame-Retardants-Including-MgOH2, 2022. (Accessed 10 February 2026).

[2] S. Kim, Flame retardancy and smoke suppression of magnesium hydroxide filled polyethylene, J. Polym. Sci. B Polym. Phys. 41 (2003) 936–944, https://doi.org/10.1002/polb.10453.

[3] H. Zhang, H. Wang, H. Wang, Flame retardant mechanism and surface modification of magnesium hydroxide flame retardant, in: IOP Conf. Ser. Earth Environ. Sci., Institute of Physics Publishing, 2018, https://doi.org/10.1088/1755-1315/170/3/032028.

[4] A. Gibson, M. Maniocha, The Use of Magnesium Hydroxide Slurry for Biological Treatment of Municipal and Industrial Wastewater. https://magnesiaspecialties.com/technical-resources/The-Use-of-MgOH2-Slurry-for-Treatment-of-Wastewater-010215, 2022. (Accessed 10 February 2026).

[5] D. Jiang, Y. Yang, C. Huang, M. Huang, J. Chen, T. Rao, X. Ran, Removal of the heavy metal ion nickel (II) via an adsorption method using flower globular magnesium hydroxide, J. Hazard. Mater. 373 (2019) 131–140, https://doi.org/10.1016/j.jhazmat.2019.01.096.

[6] G. Battaglia, M. Cardella, A. Tamburini, A. Cipollina, G. Micale, Exploitation of seawater brines for the production of nesquehonite solids and CO2 utilization, J. CO_2 Util. 96 (2025), https://doi.org/10.1016/j.jcou.2025.103101.

[7] G. Battaglia, S. Romano, A. Raponi, D. Marchisio, M. Ciofalo, A. Tamburini, A. Cipollina, G. Micale, Analysis of particles size distributions in Mg(OH)2 precipitation from highly concentrated MgCl2 solutions, Powder Technol. 398 (2022), https://doi.org/10.1016/j.powtec.2021.117106.

[8] X. Song, S. Sun, D. Zhang, J. Wang, J. Yu, Synthesis and characterization of magnesium hydroxide by batch reaction crystallization, Front. Chem. Sci. Eng. 5 (2011) 416–421, https://doi.org/10.1007/s11705-011-1125-9.

[9] C. Henrist, J.-P. Mathieu, C. Vogels, A. Rulmont, R. Cloots, Morphological study of magnesium hydroxide nanoparticles precipitated in dilute aqueous solution, J. Cryst. Growth 249 (2003) 321–330, https://doi.org/10.1016/S0022-0248(02)02068-7.

[10] M. Turek, W. Gnot, Precipitation of magnesium hydroxide from brine, Ind. Eng. Chem. Res. 34 (1995) 244–250, https://doi.org/10.1021/ie00040a025.

[11] H. Dong, C. Unluer, E.H. Yang, A. Al-Tabbaa, Recovery of reactive MgO from reject brine via the addition of NaOH, Desalination 429 (2018) 88–95, https://doi.org/10.1016/j.desal.2017.12.021.

[12] A. Cipollina, M. Bevacqua, P. Dolcimascolo, A. Tamburini, A. Brucato, H. Glade, L. Buether, G. Micale, Reactive crystallisation process for magnesium recovery from concentrated brines, desalination, Desalin. Water Treat. 55 (2015) 2377–2388, https://doi.org/10.1080/19443994.2014.947771.

[13] P.H. Karpinski, J.S. Wey, 6 PRECIPITATION PROCESSES, 2002, https://doi.org/10.1016/B978-075067012-8/50008-2.

[14] Q. Yuan, Z. Lu, P. Zhang, X. Luo, X. Ren, T.D. Golden, Study of the synthesis and crystallization kinetics of magnesium hydroxide, Mater. Chem. Phys. 162 (2015) 734–742, https://doi.org/10.1016/j.matchemphys.2015.06.048.

[15] A. Alamdari, M.R. Rahimpour, N. Esfandiari, E. Nourafkan, Kinetics of magnesium hydroxide precipitation from sea bittern, Chem. Eng. Process. Process Intensif. 47 (2008) 215–221, https://doi.org/10.1016/j.cep.2007.02.012.

[16] S. Romano, S. Trespi, R. Achermann, G. Battaglia, A. Raponi, D. Marchisio, M. Mazzotti, G. Micale, A. Cipollina, The role of operating conditions in the precipitation of magnesium hydroxide hexagonal platelets using NaOH solutions, Cryst. Growth Des. 23 (2023) 6491–6505, https://doi.org/10.1021/acs.cgd.3c00462.

[17] H. Wei, W. Zhou, J. Garside, Computational fluid dynamics modeling of the precipitation process in a semibatch crystallizer, in: Ind. Eng. Chem. Res., American Chemical Society, 2001: pp. 5255–5261. doi:https://doi.org/10.1021/ie001123v.

[18] M.M. Seckler, O.S.L. Bruinsma, G.M. Van Rosmalen, Influence of hydrodynamics on precipitation: a computational study, Chem. Eng. Commun. 135 (1995) 113–131, https://doi.org/10.1080/00986449508936342.

[19] D.L. Marchisio, A.A. Barresi, R.O. Fox, Simulation of turbulent precipitation in a semi-batch Taylor-Couette reactor using CFD, AICHE J. 47 (2001) 664–676, https://doi.org/10.1002/aic.690470314.

[20] D. Piton, R.O. Fox, B. Marcant, Simulation of fine particle formation by precipitation using computational fluid dynamics, Can. J. Chem. Eng. 78 (2000) 983–993, https://doi.org/10.1002/cjce.5450780516.

[21] H.Y. Tang, S. Rigopoulos, G. Papadakis, A methodology for coupling DNS and discretised population balance for modelling turbulent precipitation, Int. J. Heat Fluid Flow 86 (2020), https://doi.org/10.1016/j.ijheatfluidflow.2020.108689.

[22] H.C. Schwarzer, F. Schwertfirm, M. Manhart, H.J. Schmid, W. Peukert, Predictive simulation of nanoparticle precipitation based on the population balance equation, Chem. Eng. Sci. (2006) 167–181, https://doi.org/10.1016/j.ces.2004.11.064.

[23] H.Y. Tang, S. Rigopoulos, G. Papadakis, On the interaction of turbulence with nucleation and growth in reaction crystallisation, J. Fluid Mech. 944 (2022), https://doi.org/10.1017/jfm.2022.516.

[24] W. Lin, J. Wan, Y. Zhang, W. Liu, K. Li, X. Yan, J. Li, S. Li, W. Liu, Y. Lin, CFD simulation of multifluid mixing and structure optimization of rotating liquid film reactor for magnesium hydroxide production, Chem. Eng. J. 523 (2025), https://doi.org/10.1016/j.cej.2025.168398.

[25] A. Raponi, D. Fida, F. Vicari, A. Cipollina, D. Marchisio, Computational fluid dynamics and population balance model enhances the smart manufacturing and performance optimization of an innovative precipitation reactor, Processes 13 (2025), https://doi.org/10.3390/pr13061721.

[26] A. Raponi, S. Romano, G. Battaglia, A. Buffo, M. Vanni, A. Cipollina, D. Marchisio, Computational modeling of magnesium hydroxide precipitation and kinetics parameters identification, Cryst. Growth Des. 23 (2023) 4748–4759, https://doi.org/10.1021/acs.cgd.2c01179.

[27] G. Battaglia, L. Ventimiglia, F. Vicari, A. Tamburini, A. Cipollina, G. Micale, Characterization of Mg(OH)2 powders produced from real saltworks bitterns at a pilot scale, Powder Technol. 443 (2024), https://doi.org/10.1016/j.powtec.2024.119918.

[28] M. Bevacqua, F. Vassallo, A. Cipollina, G. Micale, A. Tamburini, M. Papapetrou, F. Vicari, US20240238696A1, 2022.

[29] MareMag LIFE project. https://webgate.ec.europa.eu/life/publicWebsite/project/LIFE23-ENV-IT-MareMag-LIFE-101147407/innovative-marine-magnesium-minerals-for-a-circular-safe-and-sustainable-chemicals-production, 2024. (Accessed 10 February 2026).

[30] G. Scelfo, V.M. Charitopoulos, F. Vicari, A. Tamburini, D.I. Bogle, G. Micale, A. Cipollina, Surrogate-based optimization analysis and scale-up of an ultra-concentrated brine pilot treatment chain for sustainable mineral recovery, Desalination 621 (2026), https://doi.org/10.1016/j.desal.2025.119682.

[31] L. Ventimiglia, F. Vassallo, G. Lo Burgio, A. Campione, L. Cammilli, P. Vicario, G. Battaglia, F. Vicari, A. Cipollina, A. Tamburini, G. Micale, Pilot scale production of Mg(OH)2 compounds from a real industrial reverse osmosis desalination brine, Desalination 613 (2025), https://doi.org/10.1016/j.desal.2025.119052.

[32] L.A. Bromley, Thermodynamic properties of strong electrolytes in aqueous solutions, AICHE J. 19 (2) (1973) 313–320, https://doi.org/10.1002/aic.690190216.

[33] OpenFoam, (n.d.). https://www.openfoam.com/documentation/guides/latest/doc/guide-turbulence-ras-k-omega-sst.html (accessed February 10, 2026).

[34] S. Randazzo, F. Vicari, J. López, M. Salem, R. Lo Brutto, S. Azzouz, S. Chamam, S. Cataldo, N. Muratore, M. Fernández de Labastida, V. Vallès, A. Pettignano, G. D'Alì Staiti, S. Pawlowski, A. Hannachi, J.L. Cortina, A. Cipollina, Unlocking hidden mineral resources: characterization and potential of bitterns as alternative sources of critical raw materials, J. Clean. Prod. 436 (2024), https://doi.org/10.1016/j.jclepro.2023.140412.

[35] C. Cassaro, G. Virruso, A. Culcasi, A. Cipollina, A. Tamburini, G. Micale, Electrodialysis with bipolar membranes for the sustainable production of chemicals from seawater brines at pilot plant scale, ACS Sustain. Chem. Eng. 11 (2023) 2989–3000, https://doi.org/10.1021/acssuschemeng.2c06636.
[36] M. Vanni, Approximate population balance equations for aggregation-breakage processes, J. Colloid Interface Sci. 221 (2000) 143–160, https://doi.org/10.1006/jcis.1999.6571.
[37] A. Lewis, M. Seckler, H. Kramer, G. Rosmalen, Industrial crystallization: fundamentals and applications., 2015.
[38] G. Battaglia, M.A. Domina, S. Romano, A. Tamburini, A. Cipollina, G. Micale, Magnesium hydroxide nanoparticles production from natural bitterns, Chem. Eng. Trans. 96 (2022) 43–48, https://doi.org/10.3303/CET2296008.
[39] G. Battaglia, L. Ventimiglia, F.P.M. Viggiano, F. Vassallo, A. Cipollina, A. Tamburini, G. Micale, Mg(OH)2 recovery from real bitterns: a proof of concept at pilot scale, Chem. Eng. Trans. 105 (2023) 1–6, https://doi.org/10.3303/CET23105001.
[40] H. Dai, T. Han, J. Cui, X. Li, H.N. Abbasi, X. Wang, Z. Guo, Y. Chen, Stability, aggregation, and sedimentation behaviors of typical nano metal oxide particles in aqueous environment, J. Environ. Manag. 316 (2022), https://doi.org/10.1016/j.jenvman.2022.115217.
[41] M. Kosmulski, Isoelectric points and points of zero charge of metal (hydr)oxides: 50 years after Parks' review, Adv. Colloid Interf. Sci. 238 (2016) 1–61, https://doi.org/10.1016/j.cis.2016.10.005.
[42] G.A. Parks, The isoelectric points of solid oxides, solid hydroxides, and aqueous hydroxo complex systems, Chem. Rev. 65 (2) (1965) 177–198, https://doi.org/10.1021/cr60234a002.
[43] V.A. Phillips, J.L. Kolbe, H. Opperhauser, EFFECT OF pH ON THE GROWTH OF Mg (OH) 2 CRYSTALS IN AN AQUEOUS ENVIRONMENT AT 60°C, J. Cryst. Growth 41 (1977) 228–234, https://doi.org/10.1016/0022-0248(77)90050-1.
[44] A.F. Halbus, T.S. Horozov, V.N. Paunov, Controlling the antimicrobial action of surface modified magnesium hydroxide nanoparticles, Biomimetics 4 (2019), https://doi.org/10.3390/biomimetics4020041.
[45] A.I. Gómez-Merino, F.J. Rubio-Hernández, J.F. Velázquez-Navarro, J. Aguiar, Estimation of ion diffusion coefficients at the stagnant layer using TiO2 aqueous suspension zeta potential data, Soft Mater. 13 (2015) 127–137, https://doi.org/10.1080/1539445X.2015.1017769.
[46] C. Morgante, F. Vassallo, G. Battaglia, A. Cipollina, F. Vicari, A. Tamburini, G. Micale, Influence of operational strategies for the recovery of magnesium hydroxide from brines at a pilot scale, Ind. Eng. Chem. Res. 61 (2022) 15355–15368, https://doi.org/10.1021/acs.iecr.2c02935.